Steven Percy · Chris Knight
Scott McGarry · Alex Post
Tim Moore · Kate Cavanagh

Thermal Energy Harvesting for Application at MEMS Scale

Springer

SpringerBriefs in Electrical and Computer Engineering

Steven Percy · Chris Knight
Scott McGarry · Alex Post
Tim Moore · Kate Cavanagh

Thermal Energy Harvesting for Application at MEMS Scale

Steven Percy
Chris Knight
Scott McGarry
Alex Post
Tim Moore
Kate Cavanagh
CSIRO Energy Centre
Newcastle, NSW
Australia

Preface

In most sources of low-temperature waste heat, the heat is dissipated to the atmosphere due to a lack of cost-effective solutions that can efficiently convert the heat into useable electrical energy. The ability to capture this thermal energy could increase the efficiency of existing processes and machinery, supply isolated sensors, allow for extended portable electronic power supply, and much more. The aim of this Springer Brief is to summarize a very broad range of thermal energy harvesting methods, and describe the potential of applying these methods to low-cost, batch process manufactured, micro electromechanical systems (MEMS). The brief will focus on the functionality of the device, rather than the MEMS production methods. An additional motivation for the production of this Springer Brief is the rapid growth of the MEMS market, which grew to \$11 billion in 2012 and is expected to double by 2018 [1].

Chapter 1 defines waste heat and gives examples of the sources. It also presents the concept of the Carnot limiting efficiency, and defines high- and low-grade heat energy. The chapter proceeds to outline the reasoning for the potential use of MEMS for thermal energy harvesting, and compares micro to macro-scale electromechanical systems.

The most familiar form of thermal energy conversion is the combustion heat engine. Chapter 2 describes a subset of these engines that can be used for thermal energy harvesting. These processes convert a thermal difference into mechanical motion and include four common external combustion thermodynamic cycles: Stirling, Brayton, Ericsson, and Rankine. Each cycle is described in terms of thermodynamics, and theoretical and practical design. Each cycle is then assessed against the likelihood that a practical MEMS-scale device could be manufactured to match the cycle, giving examples when available.

In Chap. 3, less common thermomechanical heat engines are described. These engines also convert thermal differences into mechanical energy, but use a variety of different mechanisms. They include the two main types of thermoacoustic processes, which use a gas phase working fluid; shape memory alloys and thermomagnetic generators, which use solid material phase change properties; and hydride heat engines, which use chemical properties of solids to store hydrogen. The key details of each mechanism are described and the practicality of designing a device at MEMS scale is discussed.

Chapter 4 outlines technologies that can convert thermally generated mechanical energy into electrical energy. The discussion includes operating temperature ranges, feasibility of scaling, and production with MEMS batch processes. This chapter focuses on maximum operating temperatures and factors that limit this.

Chapter 5 details a range of devices and technologies that can convert thermal energy directly into electrical energy. These devices use a range of techniques and physical properties of materials to perform this conversion, but mostly have no moving parts in the traditional sense. The chapter explains each technique, outlines examples of use at MEMS scale, and describes the advantages and disadvantages of each technique for use at MEMS scale. The performance or potential performance of each technique is outlined where possible. Several proprietary devices are included for the sake of completeness, although little information about these devices is publically available.

Since the best solution is dependent on the specific application, it is left to the reader to decide which will be the best solutions or technologies for future research. However, this will likely depend on the availability of new materials, and a willingness to explore low-temperature heat sources.

Reference

1. Yole Développement (2013) MEMS Trends—April 2013

Contents

Chapter 1
An Introduction to Waste Heat Capture and MEMS

Waste heat is all around us. Every energetic process, regardless of its initial form (kinetic, chemical, or electrical), eventually ends as heat, which eventually degrades to ambient temperature. In many situations, the heat could be captured and converted to electrical energy. Sources of waste heat include vehicle or engine exhaust, cooking, refrigeration, the leading edge of a plane wing, electronic devices, building air conditioning, lighting, solar radiation, and even humans.

This chapter discusses typical waste heat resources and the distribution of thermal energy at various temperatures, and defines the Carnot limiting efficiency. The advantages of using micro electro mechanical systems (MEMS) technology for this application and how this compares to macro systems are also discussed.

1.1 Waste Heat and Waste Heat Resources

As predicted by the laws of thermodynamics, every joule of energy eventually degrades to heat at ambient temperature. A specific example is the relatively small amount of hot exhaust gas from a car engine that mixes with a large amount of atmospheric gas. The hot gas will eventually cool to ambient temperature, exhibiting energy at every temperature from maximum exhaust temperature to ambient.

To demonstrate the availability of low-temperature thermal energy, consider the work done by Fox et al. [1]. The authors gathered data on energy consumption as a function of the end use temperature up to 250 °C. They studied four sectors, including residential and commercial buildings, industrial processes and process steam. Although this data is a measure of how much energy was consumed at a nominated temperature, it is also a measure of how much waste energy is available. For example, the reference notes that in the United States, in 2008, approximately 1.5 exajoules (EJ) were generated in domestic cooking at approximately 250 °C. A proportion of this thermal energy escapes from the sides of the oven, and a proportion goes into heating the food. Once cooked, the food is removed and allowed to cool to an edible temperature, creating more waste heat.

Then the food is consumed and cools to body temperature, creating yet more waste heat. Of course the food itself contains energy, which a person uses to move and run bodily processes. These processes also end as thermal waste energy and other waste products. Although it would never be possible to recapture all this energy, this illustrates the enormity of low temperature sources.

Importantly, all of that energy at 250 °C eventually degrades to the *same amount* of energy at ambient temperature. Similar processes occur for other residential energy consumers, such as hot water (60 °C), low-grade swimming pool heating (30 °C), refrigeration (110 °C), and air conditioning (70 °C). These two latter cooling processes generate high temperatures at the compressor.

This analysis can be repeated for commercial properties, which have similar needs, but at different scales, to residences; industrial processes (e.g. metal production, chemicals, and food industries) and process steam production. All of these thermal loads, regardless of their generated temperature, eventually degrade to ambient thermal energy. When these loads are combined and allowed to cool to ambient energy, the black line in Fig. 1.1 is generated.

In Fig. 1.1, the energy at each temperature is normalized against the total energy available and plotted against the initial temperature. Note that all of the normalized energy (indicated by a value of 100 %) can be found at ambient temperature, which is taken as 20 °C. Half of the normalized energy (indicated by a value of 50 %) can be found at a temperature of less than 100 °C, and just 10 %
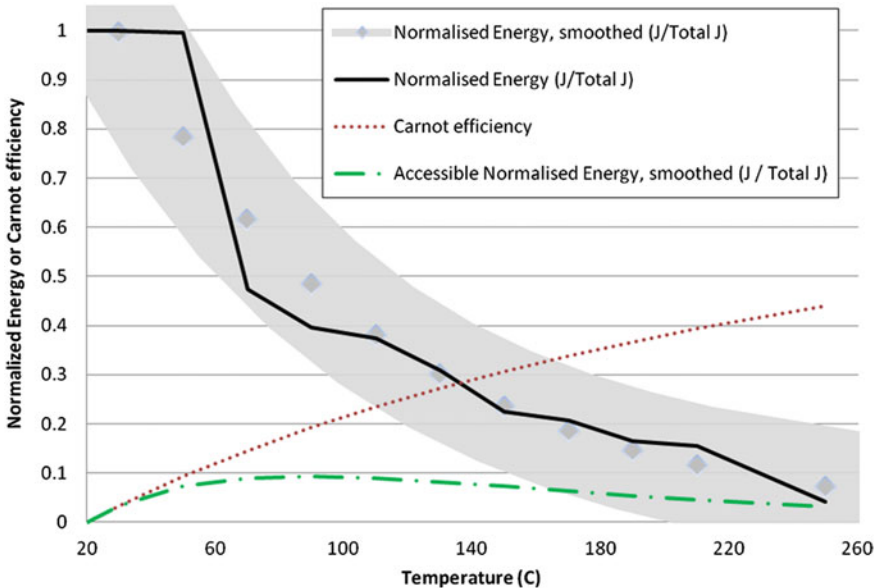
Fig. 1.1 Plot of energy availability at low temperatures, indicating the increased energy availability as temperature degrades and the effect of the cannot limit on accessible energy (data obtained from [1])

of the energy is available at above 200 °C. In this Springer Brief, we have smoothed the energy data and shown it as a thick grey band.

Although this data is presented for residential, commercial, and industrial energy consumption, the same analysis could be presented for transport energy use, in which the internal combustion engine generates waste heat from components such as exhaust gases, radiator cooling, catalytic converter heat, and manifold temperature. The shape of the curve would essentially be the same as Fig. 1.1, although the temperature range might differ; for example, catalytic converters can generate temperatures up to 1300 °C.

For a typical combustion engine, the peak thermal efficiency (η_{th}), which is the ratio of input fuel energy to output mechanical energy, is typically in the order of 30 %. What happens to the remaining 70 %? It is a consequence of the second law of thermodynamics that a heat engine must be in contact with both a hot and a cold thermal reservoir to operate, because the flow of heat between these reservoirs allows the production of power. Thus, to keep the cold reservoir cool and the system operating, heat must be constantly drawn away from the cold side of a generator. It is impossible for a heat engine to operate with no waste heat: i.e. at 100 % efficiency.

The maximum amount of energy that can be withdrawn is defined by the Carnot limit. This is often expressed as a fraction of the input power, in which case it becomes an efficiency, and is written as:

$$\eta_c = 1 - \frac{T_C}{T_H}$$

where T_C and T_H are the cold and hot reservoir temperatures in Kelvin, respectively. The dotted line in Fig. 1.1 is the Carnot limit. When the hot side temperature and the cold side temperature are the same (ambient), the Carnot limit is zero; no energy can be captured. As the hot side temperature increases, the Carnot limit also increases. Hence, the energy available for waste heat capture is the difference between the energy that has produced usable work and the energy defined by the Carnot limit. By capturing waste heat, it is possible to push an engine's efficiency closer to the Carnot limit; Fig. 1.2 shows this breakdown.

The waste heat supplied by various means of power generation and industrial processes, such as the production of alumina, cement, and steel, is often released at high temperatures (above 500 °C). This means that the waste heat can be harvested with a high Carnot limit of efficiency, and is thus termed high-grade energy. This

Fig. 1.2 Breakdown of the thermal energy available for capture
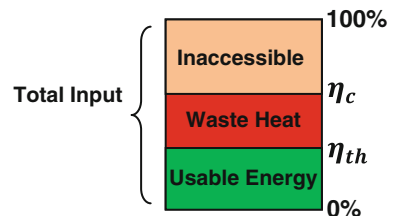
energy is easily reclaimable, and many systems are already in place to make use of it in modern industry.

However, the mid and low-grade waste heat (ambient to 250 °C) produced by various other processes usually goes unclaimed, despite accounting for more than half of the energy use of industry. In these cases, the low temperature of supplied heat means that the heat needs to be reclaimed in ways other than the large-scale turbines used in primary power production. The amount of energy that can be reclaimed at any given temperature is the product of the Carnot limit and the available energy at that temperature; this is the dot-dashed line in Fig. 1.1. For this data, there is a peak in the green line around 90 °C. This represents the maximum amount of energy available. The peak does not exceed 10 % of the total energy. Although this seems low, the total amount of energy available at 90 °C is 8.7 EJ and 3.4 EJ of this energy can theoretically be converted to useful energy.

1.2 Approaches to Waste Thermal Energy Harvesting

Several methods are currently used to harvest mid to low-grade thermal energy, including thermal-to-mechanical-to-electrical, and thermal direct to electrical. The most common methods of thermal harvesting, along with interesting novel technologies, are examined in later chapters. Both the basic principles of operation and the set of conditions leading to ideal performance vary widely between these methods, as can be seen in the following chapters.

1.3 MEMS Technology for Thermal Energy Harvesting

Micro electro mechanical systems (MEMS) describe electrical and mechanical devices sized at a few cubic millimeters or less. Within this text this is commonly referred to as the MEMS scale. In 2012, the worldwide MEMS market grew to an $11-billion business, with expected ongoing growth averaging $\sim$12.7 % through to 2018 to create a $22.5-billion market [2]. Examples of successfully commercialized technologies include acceleration sensors, optical switches, ink jet nozzles, and MEMS microphones. The emerging MEMS market—including thermal energy harvesting, micro fuel cells, MEMS speakers and MEMS ID—have been forecast to add $2.2-billion to the overall MEMS market by 2015 [2].

When applied to thermal energy harvesting, the philosophy of MEMS is to produce an extremely small, versatile method of harvesting thermal energy that can be cheaply mass-produced using methods of batch processing similar to those used to make silicon electronics; Fig. 1.3 shows a silicon wafer with multiple items printed through batch processes. Such a device could then be used to scavenge the small amounts of energy needed by low-power devices, such as wireless sensor nodes or remote control systems. Alternatively, it could be
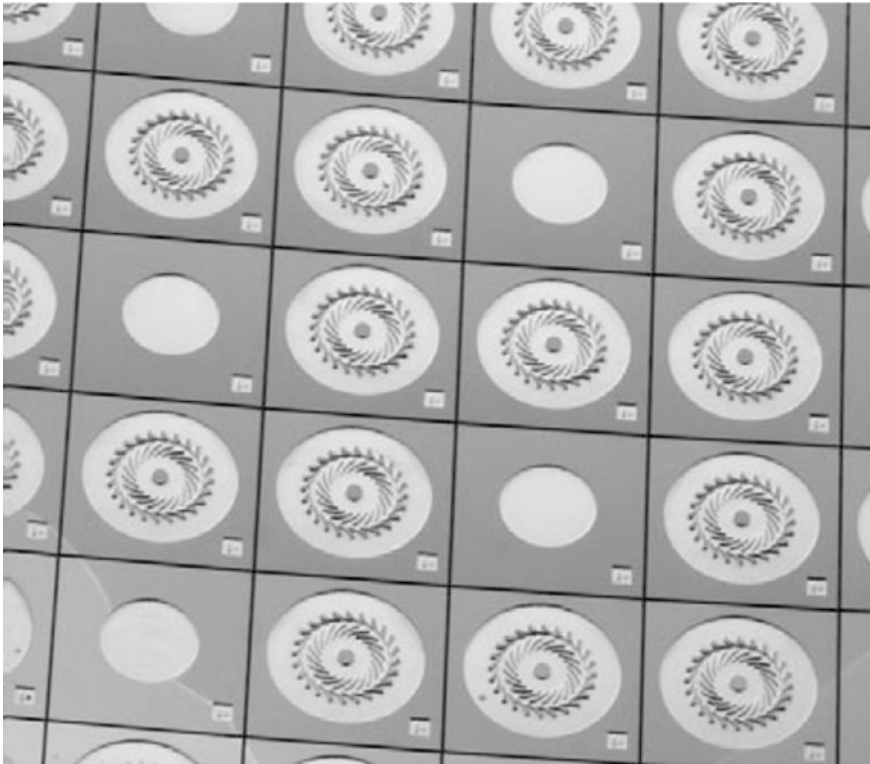
Fig. 1.3 Si wafer of radial inflow turbine stages on a single wafer. Image sourced Epstein [3], reprinted with permission from ASME. Copyright 2003, ASME

deployed in massive numbers over a wide area to reclaim a more significant amount of power for redistribution.

1.4 Macro and Micro Electro Mechanical Systems

The dominant physics of a system at macro scale, defined here as a device larger than a MEMS device, can be completely different from those at the MEMS scale. This requires consideration of micro fluidics and heat conduction, which may hamper the device or make its production impossible. In some cases, performance metrics such as cycle life and heat flow will improve; or, entirely new principles of operation may become possible, for example thermionic-tunnelling using multi-layer nanostructures [4]. The use of MEMS production technology can also enable detailed etched high-surface-area heat exchangers, allowing for a higher heat flow in a heat engine.

In this brief, a number of current thermal energy harvesting methods have been reviewed at a macro level, and then evaluated at the MEMS scale. The key characteristics examined for each system include range of operating temperatures, efficiency, and power density.

References

1. Fox DB, Sutter D, Tester JW (2011) The thermal spectrum of low-temperature energy use in the United States. Energy Environ Sci 4:3731. doi:10.1039/c1ee01722e
2. Robin L, Mounier E, Mouly J (2010) Emerging MEMS technologies & markets—2010 Report
3. Epstein AH (2003) Millimeter-scale, mems gas turbine engines. In: ASME turbo expo 2003, power for land, sea, and air. Atlanta, p 38866
4. Zeng T (2006) Thermionic-tunnelling multilayer nanostructures for power generation. Appl Phys Lett 58:153104

Chapter 2
Established Thermomechanical Heat Engine Cycles

This chapter describes and discusses the four most common external combustion thermodynamic cycles: Stirling, Brayton, Ericsson, and Rankine. Internal combustion thermodynamic cycles, such as Otto, Diesel, and rocket, will not be considered, because it is impractical to use them for waste heat capture.

A thermodynamic cycle describes the processes of transferring heat into mechanical work, through the variation of temperature and pressure. This occurs in such a way as to complete a repeatable cycle, returning to the system's initial state. For each cycle, the theorized pressure–volume (PV) diagram will be presented, along with discussions of practical macro and micro electro mechanical systems (MEMS) engines.

There are an infinite number of possible thermodynamic cycles made up of several processes. The simplest cycles are defined by just three distinct thermodynamic processes (e.g. Lenoir cycle), while other conventional cycles may have five distinct thermodynamic processes (e.g. Miller cycle). Most cycles described in this chapter are defined by four distinct processes. The Rankine cycle is the exception; it can have a variable number of processes.

2.1 The Stirling Cycle

The Stirling cycle was first proposed by Robert Stirling in the early 1800s, although has had limited application until the middle of the twentieth century. Starting in the 1950s, companies such as Ford, General Motors, Kockums and Phillips [1] developed power applications at the kilowatt scale. These have included cars [1] and submarines [2, 3]). Although the Stirling cycle matches the Carnot cycle in terms of efficiency [4], it has a number of key disadvantages inherent in a practical engine design.

Interest in the Stirling cycle at large scale has recently increased. This is, due to its attractive theoretical efficiencies, its ability to use waste heat and renewable resources such as solar concentrators, and a wide range of fuels, since Stirling

engines are externally heated. In addition, the Stirling engine is one of the few heat cycles that can be optimized for almost any temperature range.

The use of nuclear energy as a heat source in a Stirling cycle was invented by Cooke-Yarborough from the Harwell Atomic Energy Laboratories (United Kingdom) [5] in 1967. This was a very simple device, based around free-piston Stirling engines. The engine did enter production; the HoMach TMG 120 was a 300-mm-diameter device that generated 150 W at about 10 % thermal-to-electrical efficiency. The device had a total mass of less than 100 kg.

2.1.1 Theoretical Stirling Cycle

The theoretical PV Stirling cycle, shown in Fig. 2.1, is a heat cycle characterized by two isothermal reversible processes (1–2 and 3–4) and two constant-volume reversible processes (2–3 and 4–1). The first isothermal process (1–2) occurs at the high temperature side, where the working fluid is allowed to expand at constant temperature. The second part of the cycle is a constant volume process (2–3), in which the working fluid is cooled to the cycle's low-temperature point. Stage 3–4 is the low-temperature isothermal compression, in which heat is rejected from the cold side of the ideal engine. Finally, a second constant-volume process (4–1) occurs, in which heat is added to drive the working fluid back to the high temperature state.

2.1.2 Practical Macro Stirling Engines

In reality, the thermodynamic cycle shown in Fig. 2.1 can never be exactly reproduced. Instead, a practical Stirling engine will approximate this cycle. There are three common configurations that do this; these are referred to as the Alpha, Beta and Gamma Stirling engines, illustrated in Fig. 2.2.

Fig. 2.1 Pressure–volume diagram for the Stirling cycle
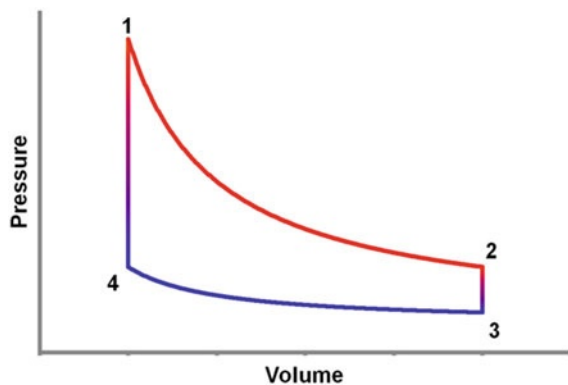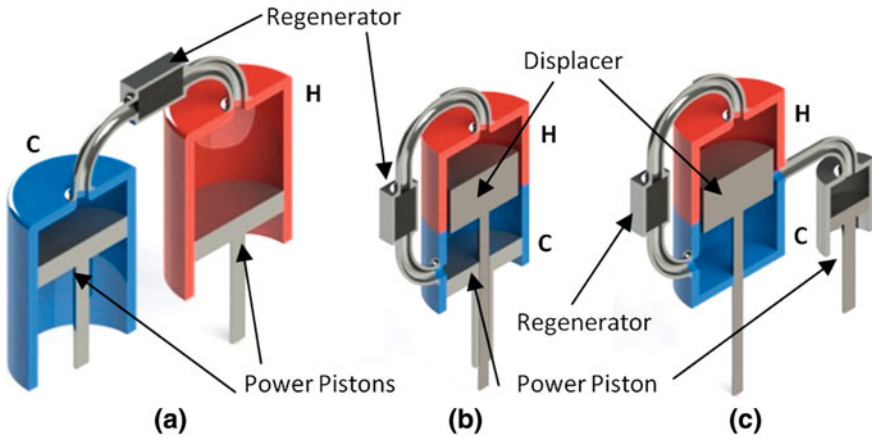
Fig. 2.2 Common topologies of Stirling engines; **a** Alpha, **b** Beta, and **c** Gamma. To follow the Stirling cycle, the pistons and displacer must be 90° out of phase

The Alpha cycle, shown in Fig. 2.2a, contains two working pistons; one for the hot side of the engine and one for the cold side. The cooling part of the cycle, in which the working volume is decreasing, causes the pistons to be drawn in. Thus, both the hot and cold side pistons need gas-tight seals. The tight seal drives up the friction losses, and necessitates higher working temperatures to achieve efficient engines.

The Beta and Gamma cycles, shown in Fig. 2.2b, c, consist of a single working piston with gas-tight seals, and a loose-fitting secondary piston (the displacer), which shuttles the working fluid between the hot and cold side. In the Beta type engine, the displacer and power piston are co-located in the same cylinder, while for the Gamma variant, the two pistons are each in their own cylinder. The reduced need for a gas-tight seal around the displacer means the losses are lower in both these types, although the Beta variant requires an additional seal where the connecting rod for the displacer passes through the power piston.

The Gamma variant has the lowest working friction. Combined with the ability to widely vary the relationship between displacer diameter and power piston diameter, this means it can be designed to be powered from very small thermal differences. A small thermal difference generates a small volumetric expansion, thus requiring a small displacement power piston relative to the swept volume of the displacer. Macro-scale designs for this style of Stirling engine can rotate from the thermal difference between ambient temperature and a cup of warm liquid, or heat emanating from human skin. At these low temperature differences, the efficiency of the system is necessarily low.

To improve efficiency, heat energy may also be stored in and rejected by a regenerator. The regenerator allows heating or cooling of the portion of the working fluid that never reaches the hot or cold side heat exchangers. Further, the regenerator allows a temperature increase or decrease of the working fluid without a change in volume (4–1 and 2–3 in Fig. 2.1). The effect of this is to maximize the

area of the temperature-limited PV diagram by filling out the corners, bringing the actual cycle closer to the ideal cycle.

Methods to improve performance include pressurizing the working fluid, and using low-specific-heat gases such as hydrogen and helium. Pressurizing the fluid increases the number of molecules in the working fluid, and low-specific-heat gases require less energy for a required temperature; pressure therefore rises. These methods require good seals where the cylinder is penetrated by pistons or piston rods.

A key advantage of the Stirling cycle is that it requires less complex mechanisms than other cycles; the designs can eliminate valves, which can impede fluid flow and increase mechanical complexity in other heat engines. Generally, the Stirling engine is quieter and more efficient at lower temperature differences and lower compression ratios. This drives a lighter design, due to the lower stresses involved.

2.1.3 MEMS Stirling Engines

Proposed MEMS implementations of Stirling refrigerators have been published, although no commercially available MEMS refrigerators are available to date. This section will outline the function of the Stirling cycle at the macro scale, and discuss some of the scientific challenges when applying this at the MEMS scale.

Due to the mechanical linkages required for the noted macro Stirling engines, they are unlikely to be useful at the MEMS scale. At the smaller scale, everyday items such as bearings, seals, and valves, can be problematic to manufacture. As such, any design that minimizes these items is likely to be easier to realize. Key to this are a variety of designs called free-piston Stirling engines. In these designs, the working fluid is completely encapsulated in a sealed volume, and power output is typically via magnets in coils or linear transducers. Cycle timing is provided by the movement of the working fluid between the hot end and the cold end, and by inertial mass and system resonance.

Published work on MEMS Stirling engines is limited, with most MEMS-scale Stirling work focused in the field of low-temperature cooling [6, 7]. This uses power input into the Stirling cycle to produce a temperature difference, rather than using a temperature difference to generate energy. Although the Stirling cycle is reversible, design optimization for refrigeration or energy generation, means that either design will probably not perform well when run in reverse.

Nakajima et al. [8] and Formosa et al. [9] both discuss miniaturization effects on efficiency and performance of Stirling engines. Nakajima et al. completes a dimensional analysis showing that as the surface area-to-volume ratio becomes larger with miniaturization, heat transfer through walls becomes more effective. Simultaneously, the ability to insulate the hot side from the cold side becomes more difficult, because they are closer together. Slide mechanisms and flywheels become problematic as friction forces begin to dominate. Formosa et al. found similar results, concluding that although specific power rises as size decreases, issues arise around sealing and friction at the piston/cylinder contact line. When a

membrane was used instead of a piston, thermal insulation between the hot and cold side fell dramatically.

At the moderate temperature range above 80 °C, Nakajima et al. [8] manufactured an engine with a swept power piston volume of 0.05 cm^3, that provided output of 10 mW at 100 °C (hot) to 0 °C (cold). The power-to-weight ratio for the design was about 1 % of a full-scale design, at about 1 W/kg [8], However, the authors suggest that this could be increased by 1–2 orders of magnitude by increasing the working fluid temperature and the hot side temperature. Efficiency may also be increased by selecting a different working fluid and increasing the working fluid pressures.

At moderate to high temperatures, a patent by Landis/NASA [6] explores the use of waste heat on board spacecraft (via radioisotope decay as the heat source) for generation of power. Although not explicitly noted, the patent indicates the intention to manufacture 'hundreds or even many thousands of individual heat engines on a single six-inch round silicon wafer'. No performance results are available, and no indication of whether the device has been realized could be found.

2.2 The Brayton Cycle

The Brayton cycle was first proposed by George Brayton in the mid 1800s. Early implementations of the cycle used pistons as the compressor and expander. The 'modern' Brayton engine has a very different configuration. It involves rotating compressor and expander fans, instead of the pistons used by George Brayton, although they follow the same cycle. These turbine engines have found large-scale use for jet propulsion, gas turbine generators and solar thermal generators. The cycle can function as an internal or external combustion engine. Its ability to function as an external combustion engine makes it of interest within this study.

2.2.1 Theoretical Brayton Cycle

By ignoring any irreversibility, the Brayton cycle can be characterized by two isentropic processes (1–2 and 3–4) and two isobaric processes (2–3 and 4–1), as shown in pressure volume (PV) and temperature–entropy (TS) diagrams in Fig. 2.3. The area enclosed by the curves indicates the work produced by the cycle.

By increasing the pressure ratio across the compressor ($P_r = P_1/P_2$) from 2 to 2′, as shown in Fig. 2.3, it is possible to increase the net work output and achieve a greater efficiency. This increase is indicated by the increased area formed by the dashed line cycle, 1–2′–3′–4. A similar cycle to the Brayton is the Ericsson cycle. The key difference is that the two isentropic processes in Fig. 2.3 are replaced with two isothermal processes. The practical effect of this is to move Point 2 horizontally to the left and Point 4 horizontally to the right on the PV diagram.
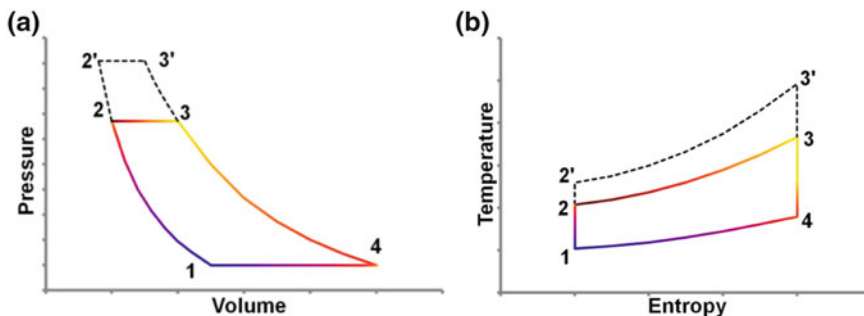
Fig. 2.3 a Pressure–volume and **b** temperature-entropy diagrams for the Brayton cycle

2.2.2 Practical Macro Brayton Engines

A practical Brayton engine following the Brayton cycle will differ from the idealized cycle shown in Fig. 2.3. This is due to irreversible effects such as stray heat transfer, friction losses, and pressure drops in the working fluid caused by fluid movement. These effects increase the work consumed by the compressor and reduce the work performed by the expander. This reduces the engine's efficiency compared with the idealized cycle.

A Brayton engine can operate as an open cycle or a closed cycle. Figure 2.4 shows both operations. Each aims to practically reproduce the theoretical cycle using a compressor, heater (heat exchanger or combustor), and expander.

In the piston or turbine configuration, the engine operates by drawing air into the compressor, in which pressure and temperature rise (1–2). The high-pressure air travels into the heater, where fuel is burned or external heat is added, which increases pressure and temperature at a constant volume (2–3). The resulting high-temperature gas then enters the expander, where it expands, performing work (3–4). In the open-cycle engine, the gas is rejected to the atmosphere. In the closed-cycle engine, the gas travels to a heat exchanger, where it is further cooled, and then fed back into the compressor (4–1).

Not shown in Fig. 2.4 is the regenerator, often used in a Brayton engine to preheat the working fluid entering the heater [10]. Less heat is then needed to bring the working fluid up to maximum working temperature. This maximizes the work produced by the heat available, increasing the efficiency of the engine.

For the closed-cycle engine, a heat exchanger is required between the expander and compressor, by reducing the fluid inlet temperature the temperature difference between the hot and cold sides of the engine is maximized, thus maximizing the Carnot limit.

It is also possible to increase the work output of a Brayton turbine when operating between two pressure levels, by expanding the gas in stages and reheating it in between. This results in a more complex PV diagram [11], with an

Fig. 2.4 Schematic of the Brayton cycle turbine or piston engine
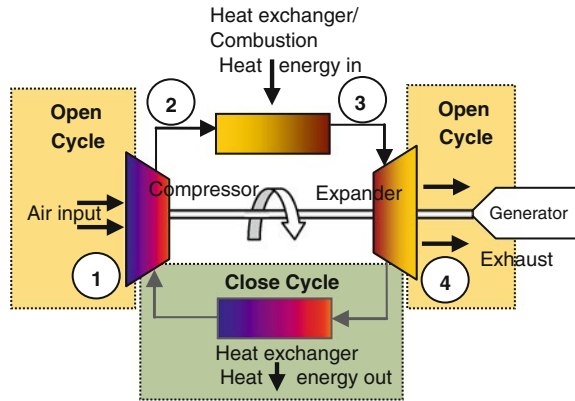
increased volume enclosed by the cycle, and hence more work is performed without increasing the maximum temperature of the cycle.

The Brayton cycle commonly uses turbines for the expander and the compressor. However, it can also use positive displacement mechanisms, such as pistons, as described by Rosa [12]. This is a closed-cycle engine that contains the same components shown in Fig. 2.4, with pistons used for the compressor and expander.

Commonly, Brayton closed-cycle engines use helium as the working fluid, because it has both high thermal conductivity and low specific heat compared with air. This increases the efficiency of the engine. The efficiency of the closed-cycle engine can be improved over a wide range of power demands by adjusting the gas pressure and heat input [13].

2.2.3 MEMS Brayton Engines

At the MEMS scale, no external heat Brayton engine has yet been developed. However, Massachusetts Institute of Technology has directed significant research into applying an internal combustion Brayton cycle turbine [14, 15]. The schematic of this engine is shown in Fig. 2.5. The authors outline many of the design challenges that would apply to both an internal and external combustion MEMS engine. These include the increased viscous forces in the fluid, reduced strength of materials, and increased surface area-to-volume ratios. The designed device consists of a series of layers, etched from silicon using photolithography [15], and stacked to form the complete engine. The device, shown in Fig. 2.6, is 20 mm in diameter and 3 mm thick, and is designed to produce approximately 10 W of output power [15]. Epstein et al. [15] claims that the power density of these devices approaches that of a full-sized Brayton turbine, although efficiency of the device still remains low.

Fig. 2.5 Schematic of H2
demo gas turbine chip. Image
sourced Epstein [14],
reprinted with permission
from ASME. Copyright 2003,
ASME
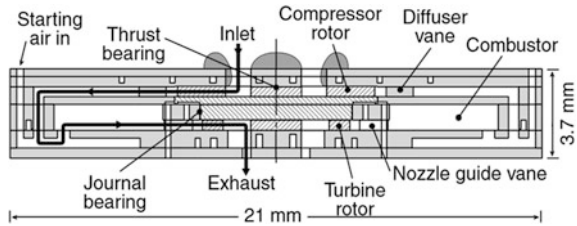
Fig. 2.6 Cutaway of the
experimental H2 demo gas
turbine chip. Image sourced
Epstein [14], reprinted with
permission from ASME.
Copyright 2003, ASME
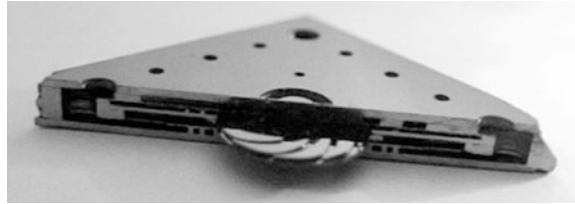
2.3 Rankine Cycle and Other Vapor Cycles

The most common vapor cycle is the Rankine cycle, named after William John
Macquorn Rankine (1820–1872). He contributed greatly to the theory of ther-
modynamics and thermodynamic processes, and was the first to fully describe the
thermodynamic process of this cycle. Most heat engines built in the eighteenth,
nineteenth and early twentieth centuries (i.e. steam engines) operate using this
thermodynamic cycle, and they kick-started the industrial revolution. The Rankine
cycle is the thermodynamic operational cycle of heat engines commonly used to
drive electrical generators, such as the steam-based cycles used in coal-fired,
nuclear, and some gas-fired power stations. Today, steam turbines produce most of
the world's electrical energy, including 90 % of electrical energy in the United
States [16]. Other novel vapor cycles exist, and will be discussed below.

2.3.1 Theoretical Rankine Cycle

The Rankine cycle heat engine uses a two-phase working fluid (liquid and gas) and
is usually a closed cycle. Within one working cycle of the engine, the working
fluid passes through both the gas and liquid phases, via the input, and then
extraction, of heat. At the cold side of the cycle, the working fluid phase is liquid,
and at the hottest point in the cycle, it is a vapor or gas. At various other periods
within the cycle, the working fluid is a combination of liquid and gas: i.e. a vapor.

Figure 2.7 shows a PV and TS diagram of a Rankine heat cycle, and Fig. 2.8
shows a schematic of an ideal Rankine cycle engine. The cycle typifies modern
steam turbine generators, in which the liquid working fluid is pressurized and
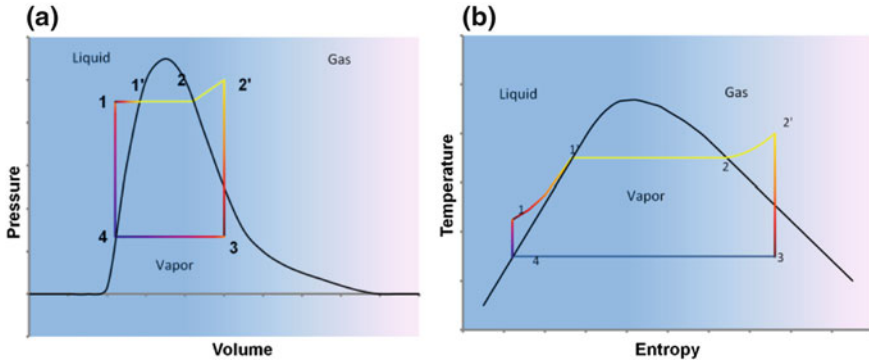
Fig. 2.7 a Pressure–volume and **b** temperature–entropy diagrams for the Rankine cycle. Points 1–4 are replicated on the schematic (Fig. 2.8). The shaded background indicates transformation from a liquid to a gas
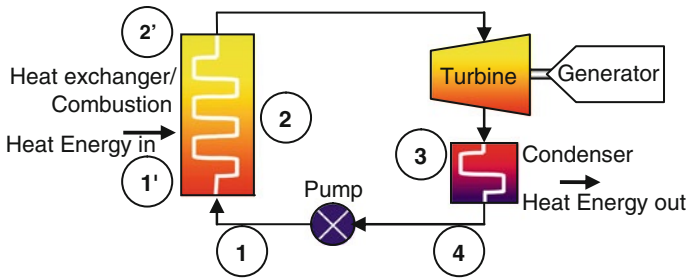
Fig. 2.8 Rankine cycle schematic

moved (by a pump, 4–1) to a heater, where it is vaporized (evaporator, 1–2) to either a high-pressure vapor (2) or a gas (2′). The vapor or gas then cools and reduces in pressure through an expander (turbine or piston, 2/2′–3) to produce useful mechanical output: e.g. to drive an electrical generator. The exhausted vapor is cooled to 100 % liquid via a reservoir or cold side heat exchanger (3–4), and then cycled back through the pump.

2.3.2 Practical Macro Rankine Engines

A common historical arrangement is that of the positive displacement, reciprocating piston engine. This engine was used to extract work from steam, as used in most steam locomotives and stationary steam engines of the eighteenth, nineteenth and early twentieth centuries. Conceptually, other arrangements of positive displacement expanders are also possible (e.g. Wankel rotor [17], scroll rotor [18], gerotor [18]).

The maximum working temperatures of macro-scale Rankine engines are limited by the materials used in their construction. The maximum working temperature is usually about 550 °C—above this, stainless steel 'creeps' (deforms permanently under a constant but relatively low stress). The minimum hot temperature, or the maximum cold temperature, at which a Rankine cycle can operate is a function of the pressure and temperature at which the working fluid changes phase.

The power density of a Rankine cycle engine, in the case of a steam engine, is in the order of 100 W/kg. The expected power level for MEMS-scale Rankine technology is about 12 kW/kg [19], with efficiencies in the range of 1–11 % [20].

Macro-scale Rankine cycle engines have achieved 47 % overall efficiency [21]. The efficiency of a modern, coal-fired, steam turbine power generator is 39 % or more [22]. For a hot operating temperature of 565 °C, and cold side temperature of 30 °C, this equates to a theoretical Carnot limit of 64 %, and therefore an overall efficiency of about 61 % of the Carnot limit at these temperatures.

A primary advantage of vapor cycles, and by inference Rankine engines, is the highly efficient pumping afforded by the use of a liquid phase at cold side temperatures. Most other heat engines that rely on a working fluid use gas only. As a result, they suffer from greater pumping losses, which may be magnified as engine speeds rise. A further advantage afforded by the Rankine cycle is the simplicity with which regeneration can be achieved. Regeneration is the transfer of heat from the working fluid after passing through an expander (e.g. turbine, piston, rotor) to the working fluid before it enters the evaporator (3–1). These advantages, combined, allow a high overall thermal efficiency.

A potential disadvantage of vapor cycles is that the properties of the working fluid must be well matched to operating temperatures and conditions. This limits the range of temperatures at which an engine operates, because the working fluid must be liquid at cold side temperatures and pressures, and reach unsaturated vapor at the hot side temperature. An unpredictable, uncontrollable, or low-grade heat energy input may render a vapor cycle engine ineffective. A well-tuned engine with controllable, predictable heat input circumvents this disadvantage. A further disadvantage of many Rankine engines—and in particular, steam turbines—is that during the expansion phase, not all of the heat energy can be extracted from the vapor. This is due to condensation of the working fluid, which contributes to blade erosion. As a result, some heat is lost through the condenser, rather than doing useful work.

2.3.3 MEMS Vapor Cycle Engines

The past two centuries have seen many publications relating to investigation and research of Rankine cycle heat engines. At the MEMS scale, Frechette and Lee have designed, built, and characterized a micro-fabricated steam turbine heat engine [19, 23]. The original concept was shown in a sketch in [19] and below in

Fig. 2.9. A recreation of the manufactured engine, including the turbine, as characterized in [23], is shown below in Fig. 2.9.

The engine uses one rotating assembly, shown in Fig. 2.10, which includes both the expansion turbine and the fluid compressing pump. The condenser is located on the lower, cold side of the device, and the evaporator on the upper, hot side. The rotor is supported by a fluid bearing, and uses the working fluid to support the mechanical loads.

The work performed by this group since 2000 includes the design and development of the system [19, 24], optimizing the bearings to support the rotating components [25], developing the rotating subsystem (including the expander turbine and the fluid pump) [23], fabricating and characterizing the device [24], and designing micro-channel heat sinks [26]. The primary advantage of this form of micro heat engine is reported as high specific power output (1–10 W per cm^2) [19], with the trade off being low overall efficiency (e.g. 7.2 %) [24]. This research group has spent more than a decade developing the device to its current state. It appears work is continuing; at the time of writing, the group's most recent articles were published during 2011 [24].

A group of researchers from Washington State University, with a number of collaborators, have developed a device they call the P^3 micro heat engine [27]. The device uses a working fluid to deflect a membrane from which energy can be extracted. It relies on the phase change of the working fluid from liquid to gas to cause expansion, and is therefore an example of a vapor cycle heat engine. The researchers have claimed:

'The prototype micro heat engine is an external combustion engine that converts thermal power to mechanical power through use of a novel thermodynamic
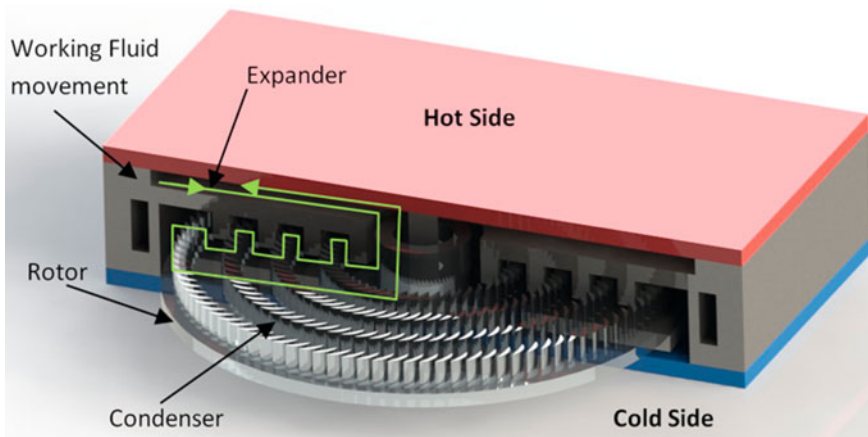
Fig. 2.9 Cross sectional schematic of experimental micro steam turbine engine [19]. The working fluid expands in the expander, does work on the turbine and condenses in the condenser. A pump on the rotor shifts the fluid back to the expander to allow for a repetitive cycle
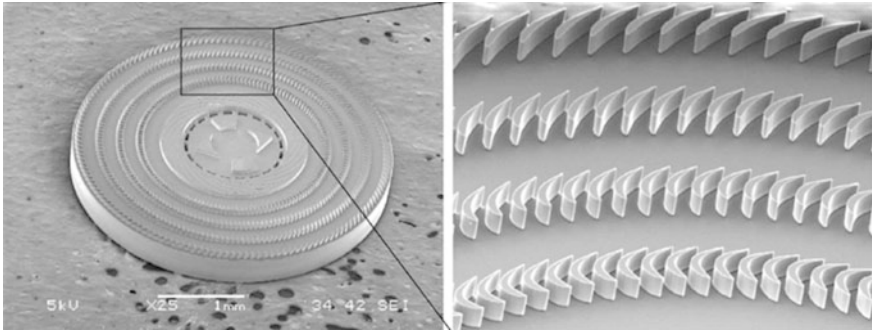
Fig. 2.10 Close-up of micro steam turbine rotor [24], note that reverse blades are located on the stator. © 2011 IEEE. Reprinted, with permission, from IEEE/ASME Journal of Microelectro-mechanical Systems [35]

cycle […] the engine consists of a cavity filled with a saturated 2 phase working fluid, bounded on top and bottom by thin membranes' [27].

Figure 2.11 shows a cross-sectional sketch of the heat engine.

The engine works via expansion and contraction of the vapor bubble (0.6 mm^3), as heat is added through the heat input resistive coil and extracted via the lower thin membrane. This causes the upper and lower membranes to deflect, due to the pressure differential between the vapor bubble and the surrounding atmosphere. When the heat input is turned off the deflection of the membrane reduces. The lower membrane is comprised of a piezoelectric membrane, which creates electrical energy upon deflection and restoration. The piezoelectric membrane can also compress the volume of the vapor bubble before heat is added.

The researchers responsible for the development of this engine claim that a primary advantage of this methodology is that 'it opens the possibility of approaching the ideal Carnot vapor cycle efficiency'.
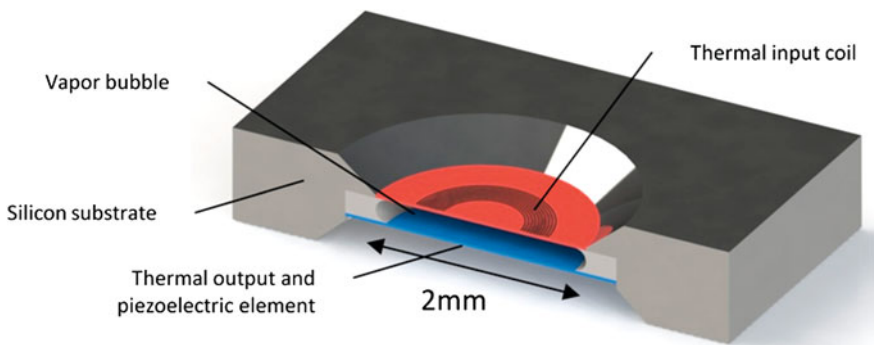
Fig. 2.11 Cross-sectional sketch of P^3 micro heat engine [27]

The research group has performed further work to improve both the engine and associated heat source. This includes fabrication and characterization of a thermal switch [28], fabrication and addition of a micro-capillary heat exchanger inside the working chamber of the engine [29], further testing of the engine including micro-capillaries and switch [30], and the addition of a Swiss roll combustor to provide a heat source for the engine [20]. From the group's 2012 publication [31], the engine was reported as producing power at 'a second law efficiency of 16 %', i.e. 16 % of the Carnot limit.

2.4 The Ericsson Cycle

The Ericsson cycle is named after John Ericsson (1803–1889), who built and patented several different heat engines using various thermodynamic principals of operation. Of these engines, some operated using what is now known as the Ericsson cycle [32]. This cycle is rarely used by modern heat engines, although there are some notable examples from the nineteenth century.

The theoretical efficiency for the Ericsson cycle is equal to the Carnot efficiency for the same limiting hot and cold temperatures. However, practical engine designs cannot match the Carnot efficiency limit.

2.4.1 Theoretical Ericsson Cycle

Analysis of a theoretical engine using gas as the working fluid shows the Ericsson cycle consists of two isothermal and two isobaric processes.

A description of an ideal Ericsson cycle engine using a gas as the working medium, as shown on the PV plot in Fig. 2.12, follows. During isothermal compression (1–2), the working gas is compressed at constant temperature. Heat is added to the gas (2–3) at a constant pressure (isobaric), normally achieved by passing the working gas through a regenerator en route to a heated cylinder. Isothermal expansion (3–4) is normally achieved by a working piston/cylinder expanding while the incoming gas is at constant temperature (the gas is pre-heated by the regenerator, with final heat addition via a heater). Isobaric rejection of heat (4–1) is again normally achieved through use of a regenerator. The regenerator absorbs the heat from the exhaust gas. The heat is then used to increase the temperature of the incoming charge of gas (2–3).

Figure 2.13 shows a schematic of one of the many variants of the Ericsson cycle. The fluid is heated at a constant pressure through the regenerator (1–2 in Figs. 2.12 and 2.13). The fluid is then expanded isothermally through a turbine, held at constant temperature by the hot reservoir (2–3). It is during this stage of the
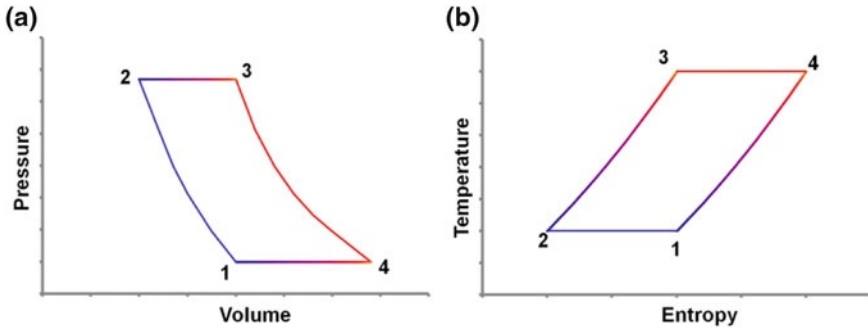
Fig. 2.12 a Pressure–volume and **b** temperature–entropy diagrams for the Ericsson cycle

cycle that energy is harvested. The working fluid is then cooled through a regenerator, at constant pressure. The heat given up at this stage (3–4) is used to heat the fluid between 1 and 2. The fluid is then compressed isothermally to its initial state through a compressor, which is held at a constant temperature by the cold reservoir. Energy input is required at this stage (4–1). This energy can be provided by direct mechanical connection to the turbine.

The two isothermal processes allow the Ericsson cycle to reach a theoretical efficiency equivalent to the Carnot limiting efficiency. As mentioned above, the regenerator allows this to occur in a practical engine, because the working gas temperature can be increased to the hot side temperature before the addition of heat from an external source. This allows the external heat to then be added at the constant hot side temperature. The corollary also holds true; the regenerator allows the exhaust gas to be cooled to the cold side temperature at constant pressure. In practice, the regenerator is simply a vessel with a large surface area and a high overall heat transfer coefficient, which allows the heat to be absorbed and rejected quickly to and from the working gas.
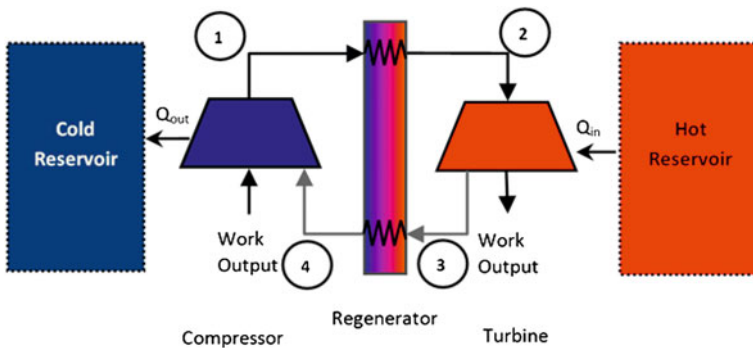
Fig. 2.13 Schematic of an ideal Ericsson cycle

2.4.2 Practical Ericsson Engines

Ericsson described the engines he produced, which operated using the basic principal of the Ericsson cycle, in patents such as [33, 34]. Although they generally followed the processes outlined in Sect. 2.4.1, these were piston engines, predominantly using air as the working gas.

The engines described in [33] are similar in concept and are each comprised of two mechanically connected pistons; a series of valves; a regenerator; mechanical linkages, to ensure the valves and pistons operate in synchronicity; a flywheel, to store and impart energy throughout the cycle; a firebox, to apply heat; and passages, to allow movement of the working gas between various parts of the engine. The engines are designed to operate in either closed or open cycle, through use or deletion of a connection pipe from the exhaust of the working cylinder to the intake of the other.

A more common example of a practical Ericsson engine is through modification to Brayton cycle engines (e.g. turbines). In these, the use of intercooling, reheating and recuperation in stages can achieve an approximation of the Ericsson cycle (see Sect. 2.2).

A further example of an Ericsson cycle device is the Johnson Thermo-Electrochemical Converter System (JTEC). While this device does not use a working gas in the traditional sense, the inventor describes it as operating on an Ericsson cycle. This device is explained in more detail in Sect. 5.5.1.

An obvious advantage of any engine that uses the Ericsson cycle is its high thermal efficiency. This is due to the two isothermal processes, during which heat is accepted and rejected at (near) constant temperature. Practically, this is not possible, but the process allows a much closer approximation of the ideal Carnot efficiency than most other engines: a notable exception being the Stirling cycle engine. Another advantage of an Ericsson engine is that it can be open cycle if using air as the working gas. This negates the need for heat sinking, because the intake air will always be at ambient temperature (maximizing the temperature difference, and therefore efficiency).

The Ericsson cycle is often compared to the Stirling cycle, due to the theoretical ability for either of them to reach the Carnot efficiency limit. However, an Ericsson gas engine is arguably more complicated than a Stirling engine of comparable performance. The traditional Ericsson engine's increased complexity is in the design and inclusion of the valves it requires to operate: in particular, the mechanical or other arrangement required to close and open the valves at the correct points in the cycle. However, these disadvantages do not appear to apply to the JTEC device, as its operation does not rely on moving mechanical components (see Sect. 5.5.1).

Late in Ericsson's career, he patented an engine [34] that operated using the Stirling cycle. The engine used an arrangement now commonly known as the Gamma Stirling engine type (see Sect. 2.1.2).

2.4.3 MEMS Ericsson Engines

The JTEC device is the only known example of an Ericsson cycle device that has been proposed at MEMS scale. See Sect. 5.5.1 for further details.

References

1. American Stirling Company (2011) Frequently Asked Questions #3. http://www.stirlingengine.com/faq. Accessed 4 Nov 2011
2. Hargreaves CM (1991) The Phillips stirling engine. Elsevier Science Pub. Co., Inc, New York
3. Anon (2011) Kockums stirling AIP system. http://www.kockums.se/en/products-services/submarines/stirling-aip-system/. Accessed 1 April 2012
4. Wark K (1989) Thermodynamics, 5th edn. McGraw-Hill, New York
5. Cooke-Yarborough E, Franklin E, Douglas W (1974) Stirling cycle heat engines
6. Nanohmics Inc., High efficiency MEMS based cryocooler. http://sbirsource.com/sbir/awards113844-high-efficiency-mems-based-cryocooler. Accessed 25 Sep 2013
7. Patterson DE, Jamison KD, Durrett M et al (2007) CVD diamond based miniature stirling cooler. In: International cryocooler conference
8. Nakajima N, Ogawa K, Fujimasa I (1989) Study on micro engines-miniaturizing Stirling engines for actuators and heatpumps. Sens Actuators 20:75–82
9. Formosa F, Chaillout J, Dessornes O (2008) Size effects on Stirling cycle micro engine. In: Proceeding of PowerMEMS, Sendai, Japan, pp 2–5
10. Earnest E, Passinos B (1979) Temperature stratified turbine compressors. US Patent 4,133,171
11. Chang H-M, Chung MJ, Lee S, Choe KH (2011) An efficient multi-stage Brayton–JT cycle for liquefaction of natural gas. Cryogenics 51:278–286. doi:10.1016/j.cryogenics.2010.10.006
12. Rosa RJ (1991) Characteristics of a closed Brayton cycle piston engine. In: IEEE Western Canada conference on computer, power and communications systems in a rural environment, pp 153–159
13. Doty D, Jones JD (1990) A new look at the closed Brayton cycle. In: Proceedings of the 25th intersociety energy conversion engineering conference, IECEC-90, vol 2, pp 166–172. doi:10.1109/IECEC.1990.716564
14. Epstein AH (2003) Millimeter-scale, MEMS gas turbine engines. ASME Turbo Expo 2003, Power for Land, Sea, and Air, Atlanta, p 38866
15. Epstein AH, Jacobson SA, Protz JM, Frechette LG (2004) Shirtbutton-sized gas turbines: the engineering challenges of micro high speed rotating machinery. J Eng Gas Turbines Power 126:358. doi:10.1115/1.1739246
16. Wiser W (2000) Energy resources: occurrence, production, conversion, use, technology. Springer, New York, p 392
17. Badr O, Naik S, O'Callaghan PW, Probert SD (1991) Rotary Wankel engines as expansion devices in steam Rankine-cycle engines. Appl Energy 39:59–76. doi:10.1016/0306-2619(91)90063-4
18. Johnston JR (2001) Evaluation of expanders for use in a solar-powered Rankine Cycle Heat Engine. Doctoral dissertation, Ohio State University, pp 1–138
19. Fréchette LG, Lee C, Arslan S (2003) Design of a microfabricated rankine cycle steam turbine for power generation. In: International mechanical engineering congress and exposition. doi:10.1115/IMECE2003-42082

20. Cho J, Lin C, Richards C (2009) Demonstration of an external combustion micro-heat engine. Proc Combust Inst 32:3099–3105
21. Henderson C (2007) Fossil fuel-fired power generation: case studies of recently constructed coal- and gas-fired power plants, 1st edn, p 176
22. Prepared by the coal utilization Research Council and the Electric Power Research Institute (2012) TLC CURC-EPRI Coal Technology Roadmap. 1–30. http://www.coal.org/usefile/file/FINAL%20Roadmap%20Report%20Update%20-%20August%202012%20%28graphics%20and%20links%29.pdf. Accessed 25 Sep 2013
23. Lee C, Fréchette L (2005) Experimental development of the rotating subsystem for a micro rankine power system. In: PowerMEMS Workshop, Tokyo, Japan
24. Lee C, Liamini M, Frechette LG (2011) A silicon microturbopump for a Rankine-cycle power-generation microsystem; Part II: fabrication and characterization. J Microelectromech Syst 20:326–338. doi:10.1109/JMEMS.2010.2093562
25. Frechette LG, Jacobson SA, Breuer KS et al (2005) High-speed microfabricated silicon turbomachinery and fluid film bearings. J Microelectromech Syst 14:141–152. doi:10.1109/JMEMS.2004.839008
26. Muller N, Frechette LG (2002) Optimization and design guidelines for high flux micro-channel heat sinks for liquid and gaseous single-phase flow. In: Proceedings of the 8th conference on thermal and thermomechanical phenomena in electronic systems, pp 449–456
27. Whalen S, Thompson M, Bahr D et al (2003) Design, fabrication and testing of the P3 micro heat engine. Sens Actuators A 104:290–298
28. Cho J, Wiser T, Richards C et al (2007) Fabrication and characterization of a thermal switch. Sens Actuators A 133:55–63. doi:10.1016/j.sna.2006.03.033
29. Whalen SA, Richards CD, Bahr DF, Richards RF (2007) Characterization and modeling of a microcapillary driven liquid–vapor phase-change membrane actuator. Sens Actuators A 134:201–212. doi:10.1016/j.sna.2006.04.038
30. Cho J, Weiss L, Richards C (2007) Power production by a dynamic micro heat engine with an integrated thermal switch. J Micromech Microeng 17:S217–S223. doi:10.1088/0960-1317/17/9/S02
31. Bardaweel H, Richards R, Richards C, Anderson M (2012) Characterization of the thermodynamic cycle of a MEMS-based external combustion resonant engine. Microsyst Technol 18:693–701. doi:10.1007/s00542-012-1496-y
32. LaGrandeur J, Crane D, Eder A (2005) Vehicle fuel economy improvement through thermoelectric waste heat recovery. In: Proceedings of the 11th diesel engine emissions reduction
33. Ericsson J (1856) Air-engine. US Patent 14,690
34. Ericsson J (1851) Engine for producing motive power. US Patent 8481
35. Lee C, Frechette LG (2011) A silicon microturbopump for a rankine-cycle power generation microsystem—Part I: component and system design. J Microelectromech Syst 20:312–325. doi:10.1109/JMEMS.2010.2093561
36. Ericsson J (1880) Air-engine. US Patent 226,052

Chapter 3
Other Thermomechanical Heat Engines

In Chap. 2, the discussion centered on traditional heat engine cycles that were developed at large to very large scale for industrial power generation. This chapter discusses smaller scale methods of converting a thermal difference into mechanical energy that are applicable at a micro-electro mechanical systems (MEMS) scale. The methods examined include thermomagnetic engines, shape memory alloy (SMA) engines, and hydride heat engines.

The process of deriving usable power from heat can be accomplished in a variety of ways. Frequently, either the only step or an initial step in this process is the transformation of heat flow into mechanical energy, in the form of motion or material strains.

The key principle behind conversion of thermal into mechanical power lies in having a reversible, thermally dependant property: e.g. gas expansion (thermoacoustic), strain (SMA), or ferromagnetism (thermomagnetic). In common with the technologies discussed in Chaps. 1 and 2, two thermal reservoirs are required, with the process sending heat from the hot reservoirs to the cold, and extracting usable work.

3.1 Thermoacoustic Heat Engines

A thermoacoustic heat engine is an external heat engine that generates mechanical energy in the form of an oscillating acoustic wave within the engine's working fluid. These engines have no need for moving parts or valves. They can operate in reverse to convert mechanical energy into a thermal difference for cryogenic coolers [1]. Within this study, the ability to convert thermal energy to mechanical energy is of interest. The thermoacoustic engine involves the same cycles that occur in a standard heat engine, such as compression, heating, expansion, and cooling [2]. Thermoacoustic engines can be divided into two categories: travelling wave devices, which can be best described by the Stirling cycle [2–5], and standing wave devices, which can be described by the Brayton cycle [1, 6]. Energy can be extracted from the acoustic energy using a diaphragm or piezoelectric transducer at one end of the thermoacoustic tube.

3.1.1 Thermoacoustic Travelling Wave Heat Engines

Travelling wave devices consist of a regenerator, hot side heat exchanger, two ambient heat exchangers and a resonator tube [7]. An example is shown in Fig. 3.1. The thermal buffer component of the travelling wave heat engine provides the heat transfer between the hot heat exchanger and ambient temperature and pressure [8].

Discussed by Ceperley in [2], and elaborated on here, is a description of how this thermoacoustic engine follows the Stirling cycle. In the following description, the numbers correspond to the cycle in Fig. 2.1, Sect. 2.1.1.

The engine operates by amplifying an acoustic pressure wave travelling from the cold to the hot side of the device. This pressure wave moves the working fluid from the cold to the hot end. The resulting increase in temperature causes the pressure to increase (compression, 4–1). The gas flows towards the hot end (heating, 1–2), followed by a pressure drop as the fluid expands (expansion, 2–3) and a transfer of the heat energy back to the cool side (cooling, 3–4). Since the travelling wave pressure is required for the Stirling cycle, the device must be tuned so that energy is always added in phase with the input travelling wave, thereby amplifying the wave.

In this cycle, the travelling wave acts as the displacer, while the standing wave through the regenerator acts as the power piston. Despite the simplicity of the design, the engine is limited by the large thermal differences required to operate at

Fig. 3.1 Section view of a thermoacoustic travelling wave heat engine
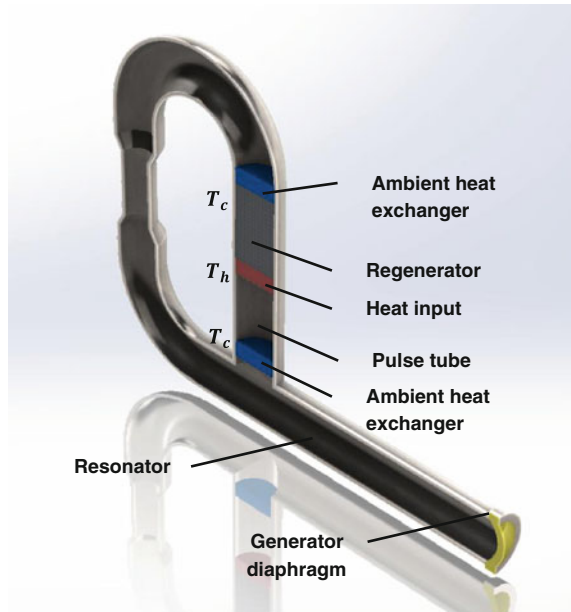
a high efficiency. Results in [4] show that for a hot gas temperature of $\sim$725 °C, a thermal efficiency of 30 % was achieved, which is 41 % of Carnot limit.

3.1.2 Thermoacoustic Standing Wave Heat Engines

Standing wave thermoacoustic devices have the same components as a common Brayton cycle engine (Fig. 2.4); a compressor, heat exchanger, expander and regenerator. However, these components operate in the configuration shown in Fig. 3.2, using a tube and acoustic pressure. A thermal gradient is set up in the wall along the length of the heat engine. This is necessary for the thermoacoustic effect to occur [6]. The cycle encourages the formation of the temperature gradient.

In this description, which expands on that given by Petculescu et al. in [6], the numbers correspond to the pressure–volume (PV) plot in Fig. 2.3, Sect. 2.1.1. When gas pressure increases towards the hot side, the following occurs. First, gas is compressed by the standing wave anti-node and an increase in temperature (compression, 1–2), since the local temperature of the wall is higher than the gas. Heat then flows from the wall into the gas, forcing it to expand (heat addition, 2–3). The high pressure gas expands, occupying a higher volume at a lower temperature. Due to the long thin design of the regenerator stack the volume of gas expands to the cold side, and as a result, reduces in temperature (expansion, 3–4). The gas then cools down, due to the local temperature of the wall, which forces the gas to contract and reduce in pressure, completing the cycle (heat rejection, 4–1). This process results in a node at the end of the thermal acoustic tube. Since this cycle sets up a standing wave in the tube, the acoustic wavelength is defined by the dimensions of the tube. Because the thermal gradient runs the length of the tube, conduction of heat into the outside environment causes an efficiency loss. As a result, standing wave devices are less efficient than travelling wave alternatives.

Fig. 3.2 Section view of a thermoacoustic standing wave heat engine
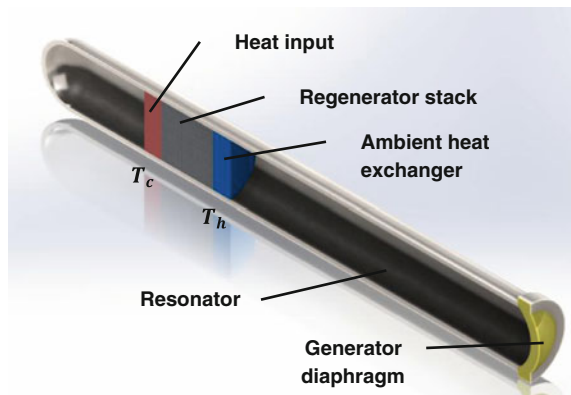
3.1.3 Thermoacoustic Heat Engines at MEMS Scale

Since thermoacoustic heat engines require oscillating working fluids for operation, the fluidic effects of scaling to MEMS will have to be taken into account. At present, no experimental thermoacoustic heat engine uses MEMS technology. However, Serry et al. [5] presents a finite element analysis of a standing wave thermoacoustic heat engine at the MEMS scale, which discusses construction methods of the proposed heat engine. The simulation shows that for a temperature difference of 80 °C across the stack, a Carnot limit of 27 % of the input energy is available. The article does not provide any practical results or experiments.

3.2 Shape Memory Alloy Heat Engines

Shape memory alloys (SMAs) are materials that recover their original shape after undergoing deformation by heating/cooling or strain/stress [9]. Hence, they having a shape 'memory'. This property was first observed in gold–cadmium alloys in the 1930s [10], and in copper–zinc alloys. However, the discovery of a nickel–titanium (NiTi) alloy, Nitinol (from Nickel Titanium-Naval Ordnance Laboratory), in 1959 [11] has received the most interest for a greater number of applications. SMAs are of interest within this study, because they provide a method of generating mechanical motion from a varying thermal input, and have characteristics desirable at a MEMS level.

The shape memory effect (SME) that these alloys undergo is achieved through a process called martensitic phase transformation. The alloys can be 'trained' to remember a configuration through forming and constraining the SMA in a desired shape and annealing at a prescribed temperature. This rearranges the dislocations present in the SMA, and allows the material to take on a new shape without internal stresses. It can also allow the SMA to be pliable at low temperatures [12]. Figure 3.3 shows the martensitic phase transformation for an example SMA. This cycle, described in [10], includes transformation via cooling from the martensite start temperature (Ms) to the martensite finish temperature (Mf). The recovery—reverse transformation—occurs on heating. The martensite persists to a higher temperature (hysteresis gap between 2 and 50 °C), then at the austenite start temperature (As), undergoes the transformation. The transformation ends at the austenite finish temperature (A_f). Due to the hysteresis, some of the mechanical energy is lost in this process, and the austenite form is generally higher strength than the martensite form [13]. Where a material can memorize two different configurations, or shapes, in the martensite and austenite phases, the behavior is called two-way shape memory [14].

The current interest in SMAs such as Nitinol is due to their ability to be produced in thin films [16]. This allows them to have potential for batch fabrication [17]. Additionally, as films, they are attractive materials for MEMS

Fig. 3.3 Example of the martensitic phase transformation in a nickel–titanium shape memory alloy showing the hysteresis loop (figure adapted from [15])
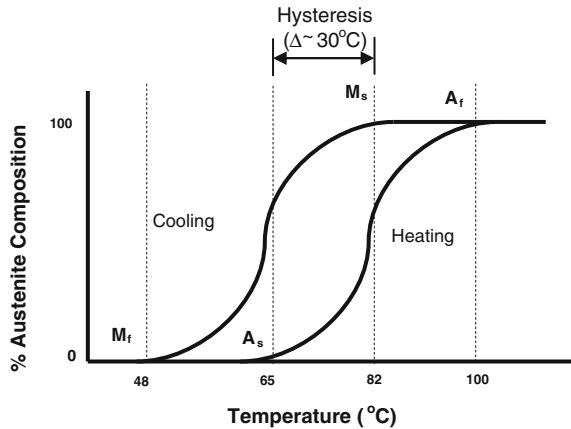
fabrication in a heat engine application. NiTi is commonly used in robotics as a micro actuator, because it is less brittle and capable of maximum recoverable strains (about twice that of the copper-based alloys) [10]. As a thin film, it contains only a small amount of thermal mass that needs to be cooled. Thus, the cycle time can be decreased and the speed of the operation increased significantly [18]. Other areas in which research and development can influence the uptake of SMAs at MEMS scale include microstructure applications, thin film quality, heat treatment compatibility and thermo-mechanical modeling [18].

NiTi alloys have a limited cycle life. At very large strains, their SME degrades significantly: from millions of cycles at 0.5 % strains to a few hundred cycles at 5 % strains, depending upon the alloy composition and conditioning. Furthermore, NiTi fibers have low efficiency (<5 %), but a great work density (>1 MJ/m^3) [15].

Some other alloys, such as copper–zinc–aluminum, are much cheaper than NiTi. However, NiTi has reduced voltage requirements, due to much higher expansion magnitudes; when including processing and running costs, this makes NiTi a better choice for cyclic applications. Thin-film SMAs have a potential work output per volume that exceeds other similar mechanisms [18]; their peak energy density is in the range of 10 MJ/m^3 and power per unit mass, 50 kW/kg [15]. SMAs can also exert a very large force per unit area (in excess of 200 MPa) and can operate at very high strain rates (300 %/s) [15]. NiTi SMAs can also undergo relatively large deformations (>5 % for poly-crystalline NiTi) [15].

The martensitic phase transformation can be actively controlled by using the SME characteristics, via thermal activation (temperature-induced transformation). Passive control uses stress-induced phase transformation at temperatures higher than A$_f$, and can provide a corrective force or movement at an appropriate working temperature (i.e. thermal cut-off values) [14]. One method of heating to induce the SME is to use electrical resistivity to pass an electrical current either directly through the SMA (applicable to small-diameter SMA wire or springs), or through a high-resistance wire or tape wrapped around the SMA (applicable to bulk SMA)

[19]. Another method is through heat transfer—by hot air, or water, or exposure to thermal radiation—which is dependent on the thermal conductivity of the SMA [19].

The contraction time of SMAs is governed by the speed of the martensitic to austenitic phase transformation. The use of very large current pulses can reduce this contraction time to several milliseconds. The contraction and expansion cycles of SMAs are mainly limited by the time required for the alloy to cool and return to its lower-temperature shape. The cooling time is determined by thermal diffusion and convection. Thus, factors such as heat capacity, latent heat involved in the phase transformation and the structural composition of the SMA are important to consider. Use of water cooling and nucleate boiling can dramatically reduce cooling time, enabling millisecond response times [15].

3.2.1 Shape Memory Alloy Heat Engine at MEMS Scale

A proposed macro-scale Nitinol-based engine, which harvests thermal energy from the alternating flow of hot and cold water over the device, has been outlined by Kauffman et al. [11]. The potential design of this engine at MEMS scale would likely make use of SMA thin-film technology. Design of an SMA heat engine consisting of a single TiNi thin-film cantilever has been proposed [20] (see Fig. 3.4). The cantilever beam is heated through contact with a heat source. The contact is maintained by a spring load applied to the tip of the cantilever.

Fig. 3.4 Proposed shape memory alloy (SMA) heat engine [10] (**a**) SMA metal after martensitic transformation. (**b**) SMA metal after austenite transformation
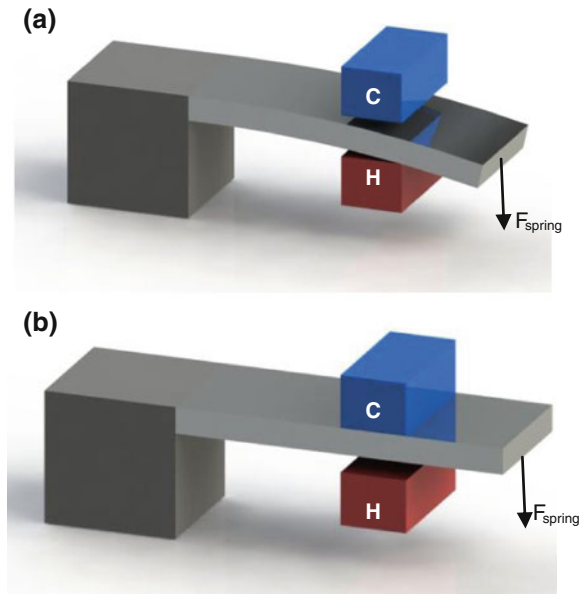
The material of the cantilever undergoes an austenitic phase transformation and moves to a horizontal position, thus losing contact with the heat source, and doing work against the spring. The beam then cools, causing a martensitic transformation. This allows the beam to flex, under the load, toward the heat source. The temperature range across which the transformation occurs determines the effectiveness of the cycle. If the thermal-displacement gradient is high for the material, the heat engine can operate within a relatively low temperature difference (as low as 20 °C) [20]. This has ideal potential for MEMS applications.

3.3 Thermomagnetic Generators

Thermomagnetic generators rely on the change in magnetization of various materials that occurs with a change in temperature. The resulting change in the magnetic field of the material can apply force to nearby magnetic objects creating mechanical work, or can create currents in nearby conductive materials creating electrical power.

The theoretical performance of thermomagnetic generators has been examined by several papers since the late 1940s. The general consensus is that their theoretical thermal-to-electrical conversion efficiency could at least equal that of modern thermoelectric devices [21–23]. Initial experimental efforts were hampered by the lack of strongly magnetic materials, and materials with relevant properties close to ambient temperature: both of which have since been discovered. Despite this, the field has received much less attention than other technologies, and experimental results backing up the theoretical predictions are yet to be realized.

In operation, a thermomagnetic generator alternately heats and cools a magnetic material by bringing it into contact with thermal reservoirs of different temperatures. This can be done actively, in designs such as that presented by Solomon [21], or passively, as demonstrated by [24].

The passive case can be used as a simple example to explain the cycle of thermomagnetic generation. In this case, the material's changing magnetization is used to actuate its movement between reservoirs. This is accomplished using a permanently magnetic hot reservoir and a restoring force—by a spring or other means—onto a cold non-magnetic reservoir. When in contact with the cold reservoir, the magnet cools due to thermal conduction, increasing its magnetization. This eventually leads to a magnetic force strong enough to overcome the restoring force, and causes the magnet to move to the hot reservoir. The magnet then heats up, losing magnetization, which causes the magnetic force to drop below the level of the restoring force. Under the force of the spring, the magnet returns to the cold reservoir, completing the cycle. This is illustrated in Fig. 3.5.

In contrast, the active case uses an external force to move the magnet between reservoirs, and the external magnetic field is cycled using electromagnets. The magnetic susceptibility of ferromagnets is dependent on temperature. This means that the change in magnetization is greater when the ferromagnet is at a low
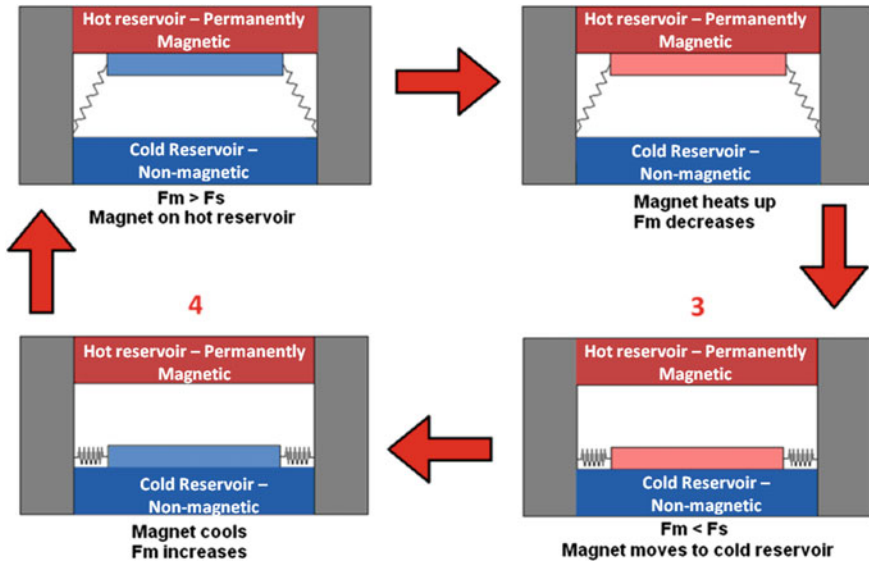
Fig. 3.5 Illustration of a basic thermomagnetic cycle indicating Fm, the magnetic force, and Fs, the restoring spring force

temperature than at a high temperature. Thus, by cooling a ferromagnet and applying an external magnetic field, then heating and removing the magnetic field, a net conversion of energy takes place from thermal to magnetic. The energy can then be harvested via induction. The basic design of a thermomagnetic generator using active magnet actuation is illustrated in Fig. 3.6, and the cycle is graphically depicted in Fig. 3.7.

Fig. 3.6 An actively controlled thermomagnetic generator
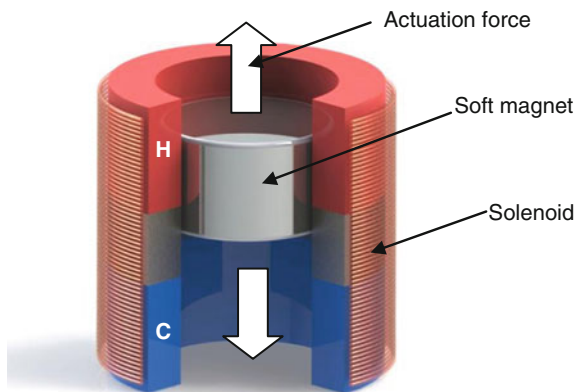
Fig. 3.7 The different magnetizations of a ferromagnet when it is cold and hot result in a net energy output when the magnetic field strength is cycled

Traditionally, designs of both passive and active thermomagnetic generators have focused on the use of ferromagnetic materials at temperatures close to the Curie point (the temperature at which a Ferromagnet loses its magnetization). This is the region in which the internal magnetization of a ferromagnet experiences the greatest change with respect to temperature, causing high thermal-to-magnetic conversion efficiency. A study by Hsu et al. [22] used the magnetization curves of several ferromagnetic materials to develop theoretical conversion efficiencies between thermal and mag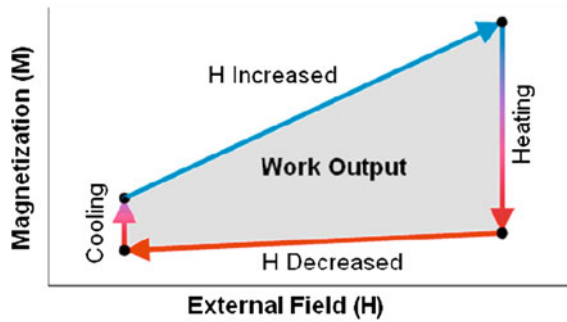netic energy. Some ferromagnetic materials were found to be capable of converting energy with theoretical efficiencies ranging from 20 to 65 % of the Carnot limit. This can be up to an order of magnitude more efficient than current thermoelectric devices. In some cases, the application was limited by either cryogenic or high Curie temperatures, necessitating operation at temperatures far from ambient (Fig. 3.8).

As mentioned at the beginning of this section, researchers have had limited success in replicating these figures experimentally. The study by Ujihara et al. [24] used a passively actuated gadolinium magnet, and converted the magnet's motion directly into electricity using a pair of piezoelectric springs. When operating between 0 and 50 °C, the device exhibited power densities of up to 3.61 mW/cm^3. This is the highest experimental power density of a thermomagnetic generator recorded to date, although it is still less than that of typical thermoelectric generators.

The performance of thermomagnetic generators is highly dependent on the parameters of the material being thermally cycled [22]. Thus, the incorporation of emerging materials into existing designs leaves room for extensive improvement on the technology's performance. For instance, a study by Srivastava et al. [25] examined the alloy $Ni_{45}Co_5Mn_{40}Sn_{10}$, which undergoes a rapid first-order phase change between a strongly ferromagnetic martensitic phase and a weakly ferromagnetic austenitic phase at a critical temperature of 130 °C. This phase change occurs over a very small change in temperature, and results in a rapid change of the material's magnetism (see Fig. 3.8).

Any thermomagnetic device must be designed for specific hot and cold reservoir temperatures. This is because specific temperatures are required for material property changes. If these are not well matched, then additional thermal energy
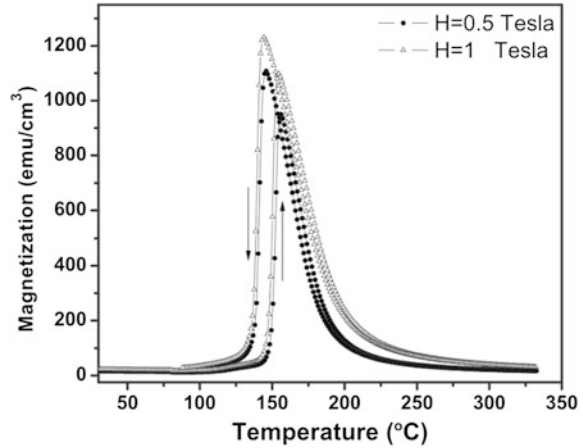
may be input without increasing energy output; or, there may be no energy output
at all.

Srivastava's experiment involved heating the alloy through its critical tem-
perature while it was surrounded by a copper coil [25]. This showed that a change
in temperature of approximately 10 °C caused a complete transformation from the
martensitic phase to the austenitic phase. The phase change increased the magnetic
susceptibility of the sample by a factor of approximately 110 (see Fig. 3.8). This
induced a peak voltage of 0.6 mV across a 2000-turn coil with a resistance of
10 kΩ between the ends. This phase change occurs much more rapidly than a
standard ferromagnetic transition at the Curie temperature. Thus, it has the
potential to greatly improve the performance of thermomagnetic generator's effi-
ciency and power output.

The emerging field of multiferroics is another area that may improve the per-
formance of thermomagnetic generators. A multiferroic material exhibits multiple
ferroic behaviors simultaneously. The three main ferroic behaviors are: ferromag-
netism, which is a spontaneous magnetization (M), reversible under an externally
applied magnetic field (H) [27]; ferroelectricity, which is a spontaneous polarization
(P) reversible under an applied electric field (E) [28]; and ferroelasticity, which is
the spontaneous strain (ε) of a material under an external stress (σ) [29].

Coupling between these behaviors may occur when they are exhibited simul-
taneously, as shown in Fig. 3.9. Such coupling is creating interest in the devel-
opment and use of new multiferroics. For instance, coupling between the
ferromagnetic and ferroelectric orders creates the phenomenon of magneto-elec-
tricity. Magneto-electricity is the spontaneous electric polarization of a material
under an applied magnetic field, or inversely, the spontaneous magnetic polari-
zation of a material under an applied electric field. Possible applications of
magneto-electricity include highly sensitive AC and DC magnetic field sensors,
current sensors, microwave resonators, and tunable devices [30].

Fig. 3.9 Simultaneous effects in multiferroic coupling
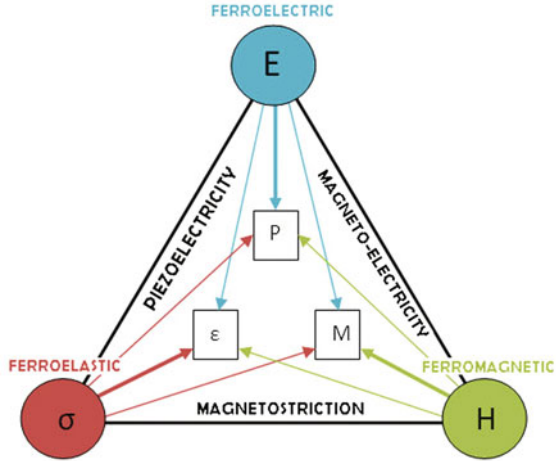
Coupling between ferromagnetism and other ferroic parameters in thermomagnetic generators would allow additional energy to be produced by the device. This could be either in the form of a spontaneous piezoelectric strain, or a spontaneous ferroelectric polarization. Many combinations of two or more of these properties simultaneously are also possible. A brief outline of some of these is given in Table 2 of [25].

3.3.1 Potential of Thermomagnetic Generators at MEMS Scale

The power density of a thermomagnetic generator increases with decreasing device size, while the thermal efficiency approaches the Carnot limit as the temperature difference between reservoirs decreases [23, 24]. Both of these behaviors indicate desirable performance of thermomagnetic generators at a MEMS scale. In addition, the operating temperature of a thermomagnetic generator would be entirely dependent upon the critical temperature of the phase changes taking place. The wide range of phase change temperatures—and the ability for these to be altered by different alloying compositions—allows for energy harvesting devices to be specially designed based on their intended operating temperature.

The study by Ujihara et al. [24] was conducted with a device of 2.4 cm^3 total volume. This remains the smallest thermomagnetic generator tested to date. Due to the simple design, the cost of producing a thermomagnetic harvester would be dominated by the material costs associated with the actual magnet, and not the surrounding device. Inexpensive ferromagnetic materials are available. However, the current cost of producing multiferroic materials is high, because they are not yet in wide use. Additionally, it is likely that the material would have to be tailor-

made for the application, since the wide variety of multiferroics, and the large dependence of their properties on composition, make it unlikely that a commercial material is currently available.

If theoretical performance can be reached experimentally, thermomagnetic generation will become a competitive method of harvesting thermal energy, and should translate well to MEMS applications. The versatility in device design of thermomagnetic generators is a key advantage of their potential as thermal energy harvesting mechanisms. With the high interest in research and development of new materials, more possibilities are continuously being created.

3.4 Hydride Heat Engine

The hydride heat engine is an engine based on the property of some special alloys (metal hydrides, e.g. $LaNi_5H_x$) to store hydrogen within their crystal lattice structure. The amount of hydrogen that metal hydrides can store is a function of the temperature of the metal hydride; the hotter the metal hydride is, the less hydrogen it can store. The metal hydride can effectively be used as a storage medium for hydrogen, with a potential storage density greater than that of carbon fiber wound compressed hydrogen tanks, if the temperature used to release the hydrogen is great enough.

When two metal hydride storage media are attached to each end of a hollow, sealed tube filled with hydrogen, the hydrogen can flow between the two storage media whenever a temperature (and therefore pressure) differential between the two media occurs. This is shown in Fig. 3.10. When one tank has the ability to store more than the other, the hydrogen flows from the tank with the lesser capacity to the tank with the greater capacity. The flow of hydrogen can drive a traditionally arranged pneumatic motor that is inserted into the closed-tube system. An electromagnetic generator can be driven by the pneumatic motor to produce electrical energy [31]. As the pressure differential between the two storage media is minimized, the potential for energy extraction diminishes. This means that as heat is being added to one medium to release hydrogen, the other must be rejecting heat as it absorbs the excess hydrogen. Further, each storage medium must be alternately heated and cooled to allow the hydrogen to continue to flow between the two media, in a reciprocating fashion. This is a particular disadvantage of this heat engine.

Another arrangement, as outlined in [32], uses four hydride storage media connected to a piston-type motor. The storage media are each successively heated and cooled using electrically controlled valves, which control the movement of a heat transfer fluid to and from the storage media. The transfer of hydrogen from and to each medium is controlled by additional electrically controlled valves. This prevents two or more media from trying to absorb and expel hydrogen at the same time, thus wasting the potential to perform work upon the piston motor.

Fig. 3.10 Schematic of a hydride heat engine
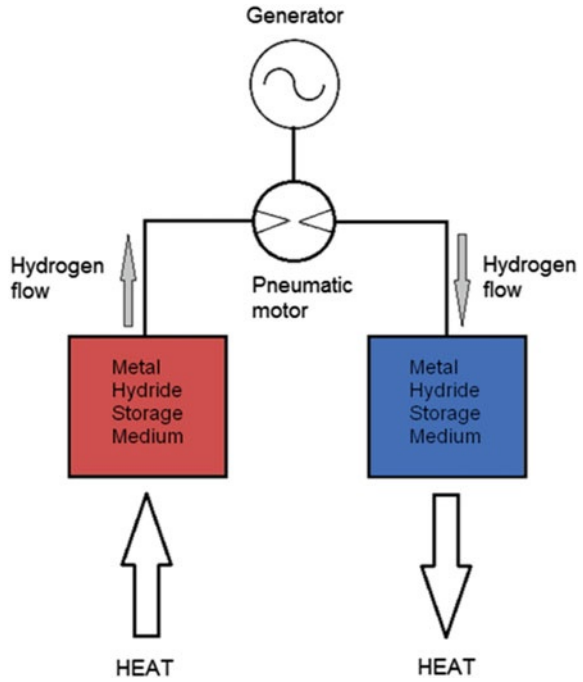
The thermodynamic cycle expressed as pressure versus volume for the device described in [32] does not match any of the 'ideal' cycles based on analysis shown in Fig. 3.11. Instead, its cycle appears unique. The power of the engine outlined in [32] is reported as 28 W average over 2 min. The experimental apparatus was significant, too large to fit on a desk; this led to a low power density.

The average conversion efficiency of the motor in [32] was reported as 7.4 % (43 % of the Carnot limit), with a theoretical conversion efficiency of 15.8 % (93 % of the Carnot limit). The working hot side temperatures used in [32] ranged

Fig. 3.11 Pressure–volume diagram for device described by Nomura et al. [32]
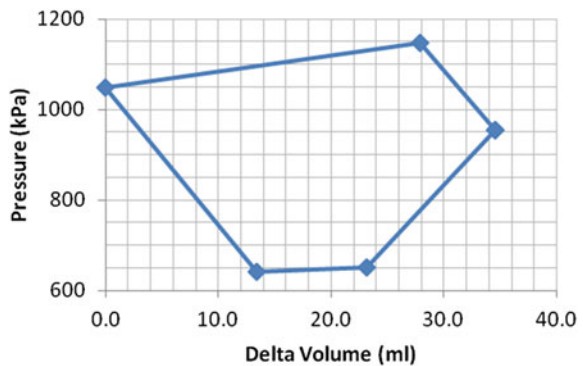
between 60 and 85 °C, with a cold side temperature of 20 °C. The relatively high efficiency and reasonably low temperature difference are advantages of this type of heat engine.

A further arrangement, as outlined in international patent WO 03/058748 A2 [33], describes a different system to extract energy from the hydride heat engine. This patent describes the use of an 'electrochemical cell', located between high and low-pressure hydrogen chambers, which allow hydrogen passing through it to generate electricity.

3.4.1 Potential of Hydride Heat Engines at MEMS Scale

Due to the complexities of alternating heat flow to and from each medium, there are few examples of such engines at the macro scale. These issues, along with additional problems such as harvesting micro-fluidic flow, will be compounded at MEMS scale. Although the potential to work at MEMS scale exists, there are no known examples.

References

1. Pierens M, Thermeau JP, Le Pollès T, Duthil P (2011) Experimental characterization of a thermoacoustic travelling-wave refrigerator. International conference on fluid mechanics, heat transfer and thermodynamics
2. Ceperley PH (1979) A Pistonless Stirling Engine—the Traveling Wave Heat Engine. J Acoust Soc Am 66:1508–1513
3. Swift GW (1988) Thermoacoustic Engines. J Acoust Soc Am 84:1145
4. Backhaus S, Swift GW (1999) A Thermoacoustic Stirling Heat Engine. Nature 399:335–338
5. Serry M, Aziz AA, Abdel-Rahman E, Sedky S (2009) A new approach for MEMS power generation based on Thermoacoustic Heat Engine. Power MEMS, pp 526–529
6. Petculescu G (2002) Fundamental measurements in standing-wave and travelling-wave thermoacoustics. PhD Dissertation, Ohio University, p 177
7. Tijani H, Spoelstra S, Poignand G (2008) Study of a Thermoacoustic-Stirling Engine. J Acoust Soc Am 123:3541
8. Backhaus S, Swift GW (2002) New varieties of Thermoacoustic Engines. Ninth international congress on sound and vibration, Orlando, FL
9. Otsuka K, Wayman CM (1998) Shape memory materials, 1st edn. Cambridge University Press, Cambridge
10. Kahn H, Huff MA, Heuer AH (1998) The TiNi shape-memory alloy and its applications for MEMS. J Micromech Microeng 8:213–221
11. Kauffman G, Mayo I (1997) The story of nitinol: the serendipitous discovery of the memory metal and its applications. Chem Educator 2:1–21
12. Yurick TJ, Mohney SE, Gray G (2001) Shape memory alloy coils optimized for electrical connectors. IEEE Trans Compon Packag Tecnol 24:389–398
13. Stoeckel D (1995) The shape memory effect—phenomenon, alloys and applications. Shape Memory Alloys for Power Systems EPRI, pp 1–13

14. Saadat S, Salichs J, Noori M et al (2002) An overview of vibration and seismic application of NiTi Shape Memory Alloy. Smart Mater Struct 11:218–229
15. Madden J, Filipozzi L (2005) Web-based actuator selection tool. Smart structures and materials 2005: Electroactive Polymer Actuators and Devices, p 9
16. Karaman I, Basaran B, Karaca HE et al (2007) Energy harvesting using martensite variant reorientation mechanism in a NiMnGa magnetic shape memory alloy. Appl Phys Lett 90:172505
17. Krulevitch P, Lee AP, Ramsey PB et al (1996) Thin film shape memory alloy microactuators. J Microelectromech Syst 5:270–282
18. Fu Y, Huang W, Du H et al (2001) Characterisation of TiNi Shape-Memory Alloy Thin Films for MEMS applications. Surf Coat Technol 145:107–112
19. Huang W (2002) On the selections of shape memory alloys for actuators. Mater Des 23:11–19
20. Wang Z, Kirkpatrick SR, Adams T, Siahmakoun A (2006) TiNi MEMS Heat Engine. In: Proceedings of SEM X international congress & exposition. Costa Mesa, CA, p 4
21. Solomon D (1991) Design of a thermomagnetic generator. Energy Convers Manage 31:157–173. doi:10.1016/0196-8904(91)90068-T
22. Hsu C-J, Sandoval SM, Wetzlar KP, Carman GP (2011) Thermomagnetic conversion efficiencies for ferromagnetic materials. J Appl Phys 110:123923–123927. doi:10.1063/1.3672844
23. Bulgrin KE, Ju YS, Carman GP, Lavine AS (2009) A coupled thermal and mechanical model of a thermal energy harvesting device. ASME 2009 International Mechanical Engineering Congress & Exposition. Lake Buena Vista, Fl, pp 327–335
24. Ujihara M, Carman GP, Lee DG (2007) Thermal energy harvesting device using ferromagnetic materials. Appl Phys Lett 91:93503–93508
25. Srivastava V, Song Y, Bhatti K, James RD (2011) The direct conversion of heat to electricity using multiferroic alloys. Adv Energy Mater 1:97–104
26. Srivastava V, Chen X, James RD (2010) Hysteresis and unusual magnetic properties in the singular Heusler alloy $Ni_{45}Co_5Mn_{40}Sn_{10}$. Appl Phys Lett 97:014101. doi:10.1063/1.3456562
27. Bozorth R (1993) Ferromagnetism, 1st edn. IEEE Press, Piscataway, p 992.
28. Seitz F, Turnbull D, Ehrenreich H (1978) Solid state physics: advances in research and applications, vol 32, 32nd ed. Academic, New York, p 341
29. Wadhawan V (1984) Ferroelasticity. Bull Mater Sci 6:733–753
30. Nan CW, Bichurin MI, Dong S et al (2008) Multiferroic magnetoelectric composites: historical perspective, status, and future directions. J Appl Phys 103:031101
31. Ergenics Solid State Hydrogen Energy Solutions Solar Powered Electric Generator. http://www.ergenics.com/page27.htm. Accessed 21 Jan 2013
32. Nomura K, Ishido Y, Ono S (1979) Novel thermal engine using metal hydride. Energy Convers 19:49–57
33. Johnson LG (2003) Electrochemical conversion system. US6709778 B2, p 5

Chapter 4
Mechanical to Electrical Conversion

While Chap. 3, describes methods to convert thermal energy to mechanical energy, this chapter will fusion an additional step to convert the themally produced mechanical energy into electrical energy. In this chapter, devices that convert mechanical energy to electrical energy will be referred to as transducers.

This chapter will explore several transducer types, from well-established and very common techniques, such as electromagnetic and piezoelectric conversion, to more niche devices, such as electrostatic transducers and the related cutting-edge technique of reverse-electro-wetting. Where appropriate, the effectiveness and efficiency of each of these techniques will be evaluated, as well as any technical issues that may limit their feasibility. In particular, this chapter will focus on the strengths and weaknesses of these classes of device when they are scaled down to the micro-electro mechanical systems (MEMS) level.

4.1 Electromagnetic Generators

Today, electromagnetic induction is the most widely used method of converting mechanical energy into electrical energy. A few examples are coal-fired power stations, wind turbines, and car alternators. The predominant reasons for the use of electromagnetic induction are the high conversion efficiency and low cost of components.

An electromagnetic generator produces a voltage across the ends of a conductor when it is subjected to a changing magnetic flux. This would normally be created using relative linear or rotational motion between a coil and a magnet [1]. The voltage generated can be used to drive a current in a closed circuit. The magnitude of the induced voltage can be defined by Faraday's equation:

$$v(t) = -\frac{N d\Phi_B}{dt}$$

where N is the number of turns in the loop, $d\Phi_B/dt$ is the time rate of change of the magnetic flux, Φ_B is the product of the magnetic field B and the area of the loop, and R is the combined resistance of the coil and the load. The magnitude of the current is defined by Ohm's law:

$$I(t) = \frac{v(t)}{R}$$

where I(t) is the current through a load, R, when a voltage, v(t), is applied. The direction of the induced current can be characterized by Lenz's law such that it establishes a magnetic flux, which opposes the change in flux linkage that gives rise to the induced voltage.

At the macro scale, electromagnetic generators can be designed to give the required voltage output for a given mechanical input. At the MEMS scale, various limitations are imposed due to processes such as sputtering and electrodeposition [2], which are commonly used for MEMS coil manufacturing. These manufacturing processes limit the number of coils that can be included in a space, due to a minimum thickness and spacing that can be fabricated [3], increase the resistance of the coil [4], and limit the ability to use complex mechanical components such as rotational parts. Together, these factors considerably reduce the efficiency of the device. If care is taken in the design, efficiency can remain relatively high; for example, Beeby et al. [5] claim 30 % conversion efficiency was achievable from their micro-electromagnetic vibration generator.

As defined by Faraday's equation above, the induced voltage is dependent on the number of turns in a coil. Due to the limitations applied to MEMS design, this limits the maximum voltage from an electromagnetic generator for a set time rate of change of the magnetic flux ($d\Phi_B/dt$). The low voltage will lead to an increased percentage loss in passive rectification and voltage boosting. Efforts can be made to increase the number of turns, using complex wiring patterns to create multilayer coils [2]. Another challenge in producing an electromagnetic generator at the MEMS scale is the batch manufacturing of a strong permanent magnet to produce the magnetic flux required for an efficient generator [6].

The operation of electromagnetic transducers is limited by temperature. Thus, when used as a mechanical-to-electrical conversion method in heat engines, electromagnetic transducers must be designed to generate energy over the expected temperature range the heat engine will endure. The limitations are due to the operating temperature of permanent magnet materials. These materials lose their magnetization above a material-specific temperature, known as the Curie temperature (see also Sect. 3.3). For an NdFeB (neodymium) magnet, a common permanent magnet type used in MEMS, the recommended maximum operating temperature is 150 °C [2]. The magnets should be operated at a temperature below this to minimize significant performance reductions.

Since the resistivity of metallic materials increases with temperature [2, 7], to reduce losses, the coil must be operated as cool as possible. This could be done by thermally insulating the coils, or locating them on the cold side of the device.

Within the MEMS field are many applications in which electromagnetic transducers harvest energy from ambient vibration. Two review articles, Arnold [8] and Hudak et al. [9] cover this research up until 2008. Arnold includes a discussion of the history and ongoing challenges for small electromagnetic generators. Hudak et al. outlines various generators developed for MEMS applications since the publication of Arnold. In these, energy is harvested from ambient vibrations, most commonly one [10] or two [11, 12] degrees-of-freedom generators.

Since these two review articles, Wang et al. [6] have developed three variations of a MEMS diaphragm-based, mass-spring-damper mechanical generator that is fully batch-fabricated. The best variation generated a voltage of 18.7 µV and an output power of 23 pW at the device resonance of 530 Hz and 9.8 ms^{-2} excitation; this corresponds to a power density of 1.6×10 nW/cm^3/g^2. Wang et al. claims that many design improvements can be made to improve the performance, including increasing the number of coil turns, positioning the magnet and coil closer, using thinner diaphragms for more compliance, increasing the centre proof mass, using strong magnets, and/or creating altogether different structures. A diaphragm of this configuration is of strong interest to a heat engine application, because it could take the place of the piston used in a conventional heat engine.

Sari et al. [11] describe a MEMS energy-scavenger module, which converts environmental vibration to a higher frequency by inducing vibration of a beam at resonance. This is done using vibration of an under-damped structure excited through a low-frequency input (70–115 Hz), resulting in oscillation of a secondary structure at 2 kHz. The design does this by supporting an NdFeB magnet using a diaphragm spring, which then moves above a series of cantilever beams that resonate at a higher frequency when released from the magnet. The device produced 15.2 mV and 11.6 pW. The design could be used when a heat engine's generated vibration frequency is low, or to improve the output when the vibration frequency changes with input thermal energy.

Jiang et al. [10] designed and tested a MEMS-based electromagnetic energy harvester, which was fabricated by bonding a vibrator with embedded micro-magnets and a stator with integrated micro coils. The micro-magnets are formed by using sputtering deposition of NdFeB/Ta multilayered magnetic films with a thickness of 10 µm, and silicon molding techniques. Results show a peak voltage of 2 mV at 115 Hz and a power density of 1.2 nWcm^{-3}. The authors identify that the performance could be greatly improved by protecting the micro-magnets from oxidation, and by decreasing the spacing between the vibrator layer and the stator layer. This emphasizes the challenge of producing generators at the MEMS scale. These processes are not yet commercialized, which limits their feasibility for large-scale production.

If a heat engine generates rotational energy, such as the millimeter-scale turbine described in [13] and discussed in Chap. 2, then a micro-rotation generator may be required. Chapter 8, by Lang et al. in [2], describes the design and testing of a

batch-fabricated, three-phase permanent-magnet induction machine. At a high rotational velocity of 305,000 rpm, a single generator can produce 8 W of rectified DC power. The authors estimate the efficiency of the generator to be 26.6 %. Losses are attributed to the viscosity of the air around the rotor, resistive losses in the coil, eddy current losses in the stator core, and to a lesser extent, hysteresis losses in the stator core.

In summary, electromagnetic generators have two main challenges: low voltage generation, and the limiting maximum operating temperatures of present magnet technologies. They have the advantages of potentially high efficiency and low cost of production.

4.2 Piezoelectric Generators

The piezoelectric effect is widely used within actuators, sensors and generators [14]. Materials exhibiting the piezoelectric effect will develop an electrical potential when a change in mechanical strain is applied. Conversely, these materials will mechanically deform when an electric potential is applied to them. Their function as generators is of interest within this study as a method of converting thermally generated vibrations from a MEMS heat engine. They have the advantage of being able to produce a much higher voltage than electromagnetic alternatives.

A significant limitation in implementing piezoelectric transducers in a heat engine application is set by the operating temperature of the piezoelectric ceramic. For a typical lead zirconate titanate (PZT) ceramic, this ranges from –20 °C to +125 °C [15]. Above this operating temperature, the ceramic can lose its piezo-electric properties [3]. Similar to an electromagnetic generator, if the heat engine application has a hot reservoir temperature approaching this upper limit, then care would have to be taken to insulate the transducer from the heat source. This could be done through use of materials with a low thermal conductivity, or by situating the transducer on the cold side of the device. If the temperature of piezoelectric transducers can be kept low, they have many advantages over other transducer methods. These include simplicity of design, no bias voltage, and the possibility of attaching PZT thin films to silicon substrates through batch processes such as the sol–gel method [16, 17]. Although these processes are not yet industrialized, some MEMS manufacturers are working to industrialize thin film PZT materials that are poled when deposited.

The most common application for piezoelectric generators in MEMS is harvesting energy from ambient vibrations. The prominent methods of improving the energy output in this situation are to induce bending strain on the piezoelectric crystal, and increasing the amplitude of bending by operating at the beam's resonance. This is done by attaching the PZT to a cantilever beam (either rectangular [18], trapezoidal [13, 16, 19], or membrane [20]). Figure 4.1 shows a rectangular cantilever bean with a piezoelectric transducer attached; x(t) indicates the
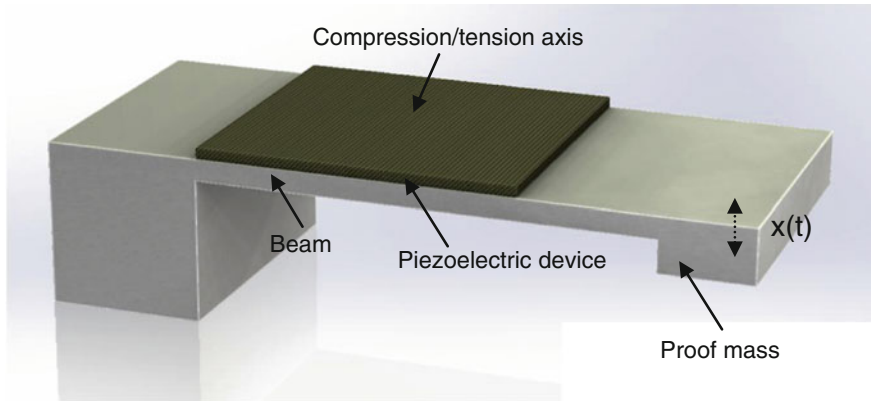
Fig. 4.1 Cantilevered beam generator

oscillating displacement that would occur. Baker et al. [19] has shown that through the use of a trapezoid instead of a rectangular structure, strain is more evenly distributed through the beam. As a result, the output power per unit volume can be increased by 30 %. This structure should also increase the cycle life of the device, due to the reduced peak strain. All cantilevered piezoelectric generator devices will have a resonant frequency at which generated power output increases significantly. For the MEMS cantilevered beam generators tested in [18], this is shown to be ~118 Hz. When used in a heat engine, this resonant nature of a cantilevered generator could have significant effect on the conversion efficiency and hence may severely limit the operating temperature range of a heat engine.

When applying piezoelectric generators to a MEMS device there are a range of opportunities that do not exist with other transducer methods such as electromagnetic and electrostatic; an example includes replacing a piston used in a macro engine with membrane with a piezoelectric material applied to the surface, similar to that used in [21].

Piezoelectric materials generate a potential in two modes: 31 and 33. Mode 31 develops a voltage perpendicular to the applied compressive or tensile; if the piezoelectric element is applied to a beam, energy is harvested using parallel plate capacitors. Mode 33 develops a potential along the same axis as the applied compressive or tensile force. In a beam bending application, mode 33 can still be used to harvest energy; this is done using top-side interdigitated electrodes. Park et al. [18] compared two MEMS rectangular cantilever beams using 31 and 33-mode PZT devices. They show that the 33-mode device exhibits a higher voltage and a lower power (7.725 V peak to peak and 0.47 μW) than 31-mode devices, which show a lower voltage yet higher power (1.35 V peak to peal and 6.72 μW). The higher voltage of the 33-mode configuration is beneficial when building passive rectifying circuitry. It is possible to increase the voltage of a the

33-mode device, which can be adjusted by changing the size of the gap between the interdigitated electrodes [18].

As discussed in Chap. 3, two publications outline the application of a piezo-electric transducer to harvest mechanical energy in a ferromagnetic heat engine: Ujihara et al. [22] and Bulgrin et al. [23]. This engine implements a piezoelectric element on two spring arms—essentially cantilevered beams—connected to a central ferromagnet. As heat is transferred from the hot side to the cold side of the device, the magnetic properties of the ferromagnet change. This causes oscillating strain applied to the spring arms and the piezoelectric element. The device shows oscillation frequencies of 2–26 Hz, depending on the pressure the device is contained within, and the oscillation gap distance used in the device [22]. This frequency is not at the resonance of the cantilever where the piezoelectric generator is attached; doing so could possibly increase the generated power. Results show a power density of 1.85 and 3.61 mW/cm^3 at a temperature difference of 50 K.

Huesgen et al. [21] outlines a model of a silicon-fabricated micro heat engine that operates through an oscillating phase change of a working fluid, due to heat transfer from the hot to the cold side of the device. This model is verified through a functional prototype. A buckling diaphragm generates the respective compressive force on the working fluid. A piezoelectric generator is integrated in the membrane; strain is applied to the generator when the phase change occurs. At a temperature difference of 37 K, the model predicts 1.29 µW at a frequency of 0.72 Hz.

4.3 Electrostatic Transducers

Electrostatic transducers can convert mechanical energy into electrical energy by using the input mechanical energy to change capacitance of the generator between a high and low value. The capacitance is most commonly reduced by increasing the distance between the capacitor plates, or by reducing the overlapping area of the plates. Electrostatic transducers operate in one of two modes. The first is constrained charge mode, in which the charge and electric field remain constant on the capacitor plates, causing an increase in voltage as the capacitance reduces [24]. The second is constrained voltage mode, which causes charge to move from the capacitor to a storage device as the capacitance decreases [25, 26].

Figure 4.2 and Table 4.1 compare the differences between the two modes. Both methods convert mechanical kinetic energy to electrical energy from work done against the electrostatic forces between the two plates. A control circuit [27] is required to bias and extract the energy from the transducer; the control and bias configuration is dependent on the mode of operation. Examples of this circuitry can be found in [24–26]. The use of biasing can be avoided by using electrets, which is a permanent charge buried in a dielectric layer [1, 28].

Electrostatic converters have the significant advantage of easy manufacture from silicon-based MEMS technology with minimal complexity. As mentioned
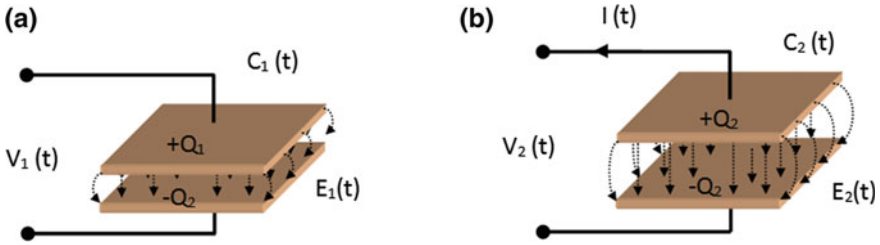
Fig. 4.2 An electrostatic transducer shown in the (**a**) low energy (**b**) high energy states. C capacitance; E electric field; I current; Q charge; V voltage

Table 4.1 Electrostatic transducer operating modes

	Constrained Q mode	Constrained V mode
Capacitance	C1(t) < C2(t)	C1(t) < C2(t)
Charge	Q1(t) = Q2(t),	Q1(t) > Q2(t)
Electric field	E1(t) = E2(t)	E1(t) > E2
Current	I(t) = 0	|I(t)| > 0
Voltage	V1(t) < V2(t)	V1(t) = V2(t)

previously, commercial MEMS production companies do not provide the option to include materials such as PZT and permanent magnets in their production processes, although they can easily produce an electrostatic transducer. This means that electrostatic transducers can be externally produced, which allows institutions without production facilities to conduct research and prototyping. The associated disadvantages are the extra complexity and volume required for the bias and energy extracting circuitry, and the high voltages generated in constant charge mode, which can be in the order of thousands of volts to obtain high power generation [24].

Since silicon can withstand high temperatures—single crystal Si melts at 1414 °C [29]—electrostatic transducers can withstand a large range of temperature differentials for heat engine applications. However, the strength of silicon degrades as the temperature increases.

Most applications of electrostatic transducers harvest energy from ambient vibration, implementing an inertial mass spring damper system with a designed resonance to target a particular vibration frequency. Roundy et al. [30] defines three device configurations that can be used for this application: in-plane overlap, where capacitance varies dependent on the overlapping area of fingers; in-plane gap closing, where capacitance varies with the gap between fingers; and out-of-plane gap closing, where capacitance varies by changing gap distance between two capacitor plates. Roundy et al. discuss the challenges of each configuration, including aspects such as fluid damping. Their dynamic simulations reveal that an output power density of 116 μW/cm^3 is possible from a vibration source of 2.25 m/s^2 at 120 Hz.

At the time of writing, no heat engines use electrostatic transducers to convert thermally generated vibrations into electrical energy.

4.4 Reverse Electro-Wetting Generators

Reverse electro-wetting is a method of converting mechanical energy into electrical energy. The principle of its operation was first published in *Nature Communications* in 2011 [31], but the idea is based on the concept of electro-wetting, which has been recognized for more than a century. In electro-wetting, micro-droplets of liquid are dispersed over an insulating surface. When a voltage is applied between a droplet and a conducting surface beneath the insulating layer, the capacitance between the two materials causes the droplet to lower the interfacial energy and flatten out [32].

Reverse electro-wetting is the reverse of the above phenomena, and functions as a liquid dielectric electrostatic transducer. Again, micro-droplets are dispersed across an insulating surface or a micro-channel with a conducting electrode beneath it; this is shown in Fig. 4.3a–c. A bias electric field is applied between the droplet and the electrode, causing charges to move in the droplet, which then
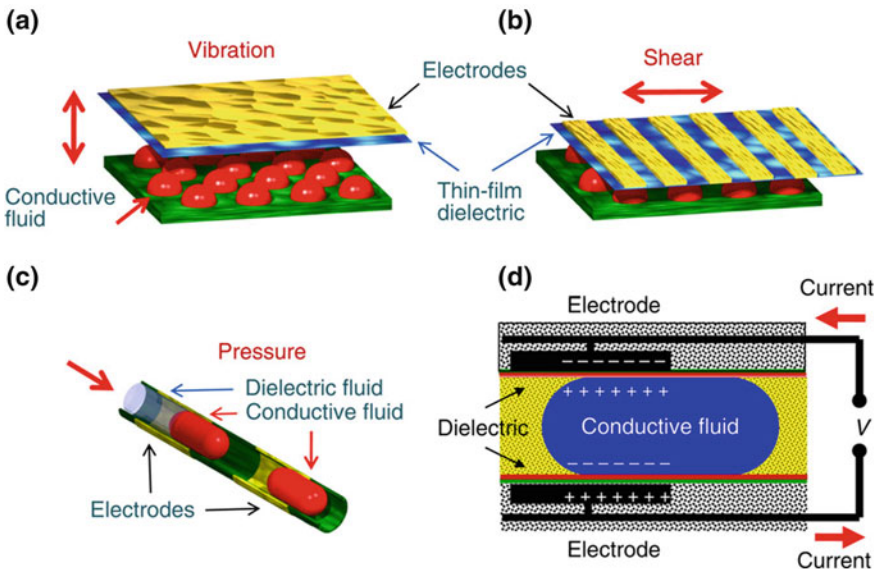

Fig. 4.3 Schematics of three major droplet actuation mechanisms. These include (**a**) droplets between oscillating plates (**b**) droplets between sliding plates, and (**c**) droplets in a micro-channel. (**d**) shows in greater detail schematics of reverse-electro-wetting-based energy generation process in a micro-channel geometry. Reprinted by permission from Macmillan Publishers Ltd: Nature Communications [31], ©2011

accumulates at the border with the dielectric layer. External mechanical actuation can then be used to move the droplet such that the area of overlap with the electrode is decreased. This reduces the capacitance of the field and causes electric current to flow, in the same method as that used in an electrostatic transducer given in Sect. 4.3. While no MEMS heat engine using this technique has been demonstrated to date, it may be possible to select the operating temperature of the liquid to allow it to operate as a transducer method over a wide temperature range.

Reverse electro-wetting at the time of writing is still in the very early stages of development. As such, it is yet to be successfully applied to the field of thermal energy harvesting. Krupenkin et al. [31] have demonstrated typical energies as high as 0.4 μJ/mm^2 per oscillation. They have also patented a design [33] for development of the energy harvesting device, with a projected application being human movement energy harvesting. Their projected energy generation from this device is approximately 10 W using a bias voltage of 35 V [31]. Possible thermal harvesting applications could include harvesting energy from fluid convection flow, or coupled with oscillatory systems, as discussed in Chap. 3.

References

1. Mitcheson PD, Yeatman EM, Rao GK et al (2008) Energy harvesting from human and machine motion for wireless electronic devices. Proc IEEE 96:1457–1486
2. Arnold DP, Allen MG (2010) Fabrication of microscale rotating magnetic machines. In: Lang J (ed) Multi-wafer rotating MEMS machines, pp 157–190
3. Priya S, Inman DJ (2008) Energy harvesting technologies, 1st ed. Springer, New York
4. Kulkarni S, Koukharenko E, Torah R et al (2008) Design, fabrication and test of integrated micro-scale vibration-based electromagnetic generator. Sens Actuators, A 145:336–342
5. Beeby SP, Torah RN, Tudor MJ et al (2007) A micro electromagnetic generator for vibration energy harvesting. J Micromech Microeng 17:1257–1265
6. Arnold DP, Wang N (2009) Permanent magnets for MEMS. J Microelectromech Syst 18:1255–1266
7. Young HD, Freedman RA (2004) University Physics, 13th ed. Addison Wesley, New York, pp 950–953
8. Arnold DP (2007) Review of microscale magnetic power generation. IEEE Trans Magn 43:3940–3951
9. Hudak NS, Amatucci GG (2008) Small-scale energy harvesting through thermoelectric, vibration, and radiofrequency power conversion. J Appl Phys 103:101301–1013024
10. Jiang Y, Masaoka S, Fujita T et al (2011) Fabrication of a vibration-driven electromagnetic energy harvester with integrated NdFeB/Ta multilayered micro-magnets. J Micromech Microeng 095014
11. Sari I, Balkan T, Kulah H (2010) An electromagnetic micro power generator for low-frequency environmental vibrations based on the frequency upconversion technique. J Microelectromech Syst 19:14–27
12. Turkyilmaz S, Kulah H, Muhtaroglu A (2010) Design and prototyping of second generation METU MEMS electromagnetic micro-power generators. Int Conf Energy Aware Comput, pp 16–18
13. Tang G, Liu JQ, Liu HS et al (2011) Piezoelectric MEMS generator based on the bulk PZT/ silicon wafer bonding technique. Solid State Phys 208:2913–2919

14. Phillips JR (2008) Piezoelectric technology primer. CTS Wireless Components
15. Typical Parameters of Piezoelectric Ceramics (2012). http://www.piceramic.com/piezo_materials_2.php. Accessed 12 Sep 2012
16. Kim D, Park J (2010) Recent progress of piezoelectric MEMS for energy harvesting devices. Annual conference on experimental and applied mechanics: MEMS and nanotechnology. Bethel, vol 2, pp 17–24
17. Bin FH, Liu JQ, Xu Z et al (2006) Fabrication and performance of MEMS-based piezoelectric power generator for vibration energy harvesting. Microelectron J 37:1280–1284
18. Park J, Ahna H, Kim SB et al (2011) Comparison of transduction efficiency for energy harvester between piezoelectric modes. Soc Exp Mech Ann Conf: MEMS Nanotechnol 2:33–39
19. Baker J, Roundy S, Wright P (2005) Alternative geometries for increasing power density in vibration energy scavenging for wireless sensor networks. 3rd international energy conversion engineering conference. American Institute of Aeronautics and Astronautics, Reston, pp 1–12
20. Cho JH, Richards RF, Bahr DF et al (2006) Efficiency of energy conversion by piezoelectrics. Appl Phys Lett 89:104103–104107
21. Huesgen T, Ruhhammer J, Biancuzzi G, Woias P (2010) Detailed study of a micro heat engine for thermal energy harvesting. J Micromech Microeng 20:104004. doi:10.1088/0960-1317/20/10/104004
22. Ujihara M, Carman GP, Lee DG (2007) Thermal energy harvesting device using ferromagnetic materials. Appl Phys Lett 91:93503–93508
23. Bulgrin KE, Ju YS, Carman GP, Lavine AS (2009) A coupled thermal and mechanical model of a thermal energy harvesting device. ASME 2009 International Mechanical Engineering Congress & Exposition. Lake Buena Vista, Fl, pp 327–335
24. Miao P, Holmes AS, Yeatman EM, Green TC (2003) Micro-machined variable capacitors for power generation. International conference on electrostatics. Edinburgh, pp 53–58
25. Torres EO, Rincon-Mora GA (2010) Self-tuning electrostatic energy-harvester IC. IEEE Trans Circuits Syst II Express Briefs 57:808–812
26. Torres EO, Rincon-Mora GA (2010) A 0.7- μm BiCMOS electrostatic energy-harvesting system IC. IEEE J Solid-State Circuits 45:483–496
27. Meninger S, Mur-Miranda JO, Amirtharajah R et al (2001) Vibration-to-electric energy conversion. IEEE Trans Very Large Scale Integration (VLSI) Syst 9:64–76
28. Sterken T, Fiorini P, Baert K et al (2003) An electret-based electrostatic μ-generator. 12th international conference on transducers, solid-state sensors, actuators and microsystems. IEEE, Boston, pp 1291–1294
29. Materials NE About Silicon (2012). http://www.novawafers.com/resources-about-silicon.html. Accessed 11 Aug 2012
30. Roundy S, Wright PK, Pister KSJ (2002) Micro-electrostatic vibration-to-electricity converters. ASME international mechanical engineering congress & exposition. New Orleans, p 39309
31. Krupenkin T, Taylor JA (2011) Reverse electrowetting as a new approach to high-power energy harvesting. Nat Commun 2:448. doi:10.1038/ncomms1454
32. Mugele F, Duits M, Van den Ende D (2010) Electrowetting: a versatile tool for drop manipulation, generation, and characterization. Adv Colloid Interface Sci 161:115–123. doi:10.1016/j.cis.2009.11.002
33. Krupenkin TN, Madison NJ (2011) Method and apparatus for energy harvesting using microfluidics. U.S. Patent No. 8,053,914

Chapter 5
Thermal to Electrical Energy Converters

The previous chapters discussed the generation of mechanical motion from thermal energy and the subsequent conversion of this to electrical energy. The additional step from thermal to electrical energy can introduce further losses, reducing overall efficiency. In this chapter, the conversion of thermal energy directly to electrical energy is discussed.

The methods examined include thermionic, pyroelectric, and Seebeck generators, alkali metal thermal-to-electric converters, Johnson thermo-electrochemical converter, Johnson electrochemical heat pipe, and infrared photovoltaic harvesters.

5.1 Thermionic Generators

Thermionic emission features the spontaneous rejection of electrons from a hot surface [1], and is also known as the Edison effect. As the electrons of a heated material are imparted with thermal energy, they gain the ability to escape from the material's surface. The energy lost in this process is termed the work function. The work function is a property of the emitting surface, and is generally in the order of several electron volts in magnitude.

If an electron collector (anode) is placed near the material undergoing thermionic emission, the large number of free electrons incident on its surface cause it to develop an electric charge. Each electron incident on the collector also contributes energy equal to the collector's work function. Connecting the anode to the emitter (cathode) by a closed circuit allows electrons to flow back to the emitter, creating a current (see Fig. 5.1). The difference in work function between emitter and collector surfaces then becomes available as a voltage of supplied power. Thus, raising the work function of the emitter increases the voltage difference between electrodes, supplying more power. Doing this requires a much higher emitter temperature.
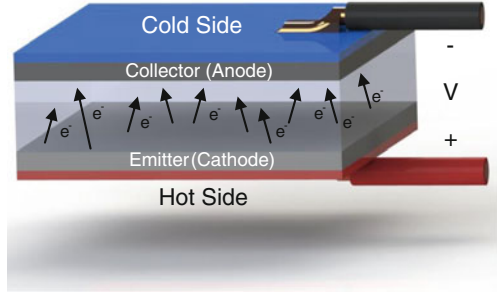
Thermionic emission is governed by two factors: the current density of electron
emission, and the transport of this current between electrodes. Electron emission is
described by Richardson's law [2]. This equation links the current density, J (A/
m^2), of thermionically emitted electrons; the work function of the emitting surface,
W (eV); the temperature of the emitting surface, T (K); and a constant, A, in the
form:

$$J = AT^2 \exp^{\left(\frac{-W}{kT}\right)}$$

where k is Boltzmann's constant, and A is given by the expression:

$$A = \frac{4\pi mk^2 e}{h^3}\lambda_0$$

with m and e the mass (kg) and charge (C) of an electron, respectively; Planck's
constant, h; and a material constant, λ_0.

The transport of electrons between the anode and cathode is governed by the
development of space-charge in the inter-electrode spacing. In a vacuum, the
density of electrons in this space creates a region of negative electrical charge, and
thus repels further electrons from making the transition, greatly reducing the
performance of the device. This is overcome in most modern thermionic gener-
ators through the use of a highly ionizable gas—normally, cesium vapor [1, 3]—
which is deposited in the inter-electrode gap. This neutralizes the space charge, as
well as adsorbing onto the electrodes and lowering their work function, greatly
improving device efficiency at lower temperatures. Neutralizing the effects of
space charge ensures that the generator is emission limited. That is, the current is
determined by the emission of electrons from the cathode, and not by the space
charge distribution between electrodes.

Thermionic generators are effectively a form of heat engine with electrons as
the working fluid, and are thus subject to the Carnot limit of efficiency. However,
since they typically have high operating temperatures (>1000 K), their theoretical
Carnot limit is high [4]. Despite this, reported efficiencies of total thermal-to-
electrical conversion for thermionic generators range from 5 to 20 % [5], but
depend largely on the operating temperature.

5.1.1 Potential of Thermionic Generators at MEMS Scale

Thermionic devices have been realized at the scale necessary for micro-electro mechanical systems (MEMS) operation, with promising results. Scaling down has been found to have a positive effect on both output power density and efficiency, as long as sufficient thermal isolation between the electrodes can be maintained [6, 7]. New developments in the use of nanometer-scale electrode gaps have also had interesting results. Decreasing the gap between electrodes to a scale of 1–10 nm allows quantum tunneling to be observed between the electrodes. This drastically lowers the effective work function of the emitter surface, allowing operation at far lower temperatures than previously attained [8]. This process, which has become known as 'thermo-tunneling', has allowed efficiencies approaching 50 % of the Carnot limit at temperatures around 800 K [5], and 30 % at 500 K; predicted power densities range up to 10 W/cm^3 [9].

Combined with the lack of moving parts, this performance makes thermionic devices suitable for MEMS-scale applications, provided that the construction materials are able to withstand the high temperatures necessary for operation. Thermionic devices are typically resilient, with working lifetimes of 7–10 years demonstrated by thermionic power modules in satellites [6].

Due to the relatively recent development of thermo-tunneling devices, cost figures are limited. However, some device developers estimate costs of US$500–1000 per installed kilowatt, based on an electrode temperature difference of 600 K [9].

Finally, thermionic devices are simple by nature, exhibit high energy densities, and produce power through the use of a necessarily small electrode gap. The main drawback of thermionic power generation is the high temperature necessary to overcome the work function of most materials. Even for thermo-tunneling devices, this limits the use of thermionics to applications at temperatures well above ambient.

5.2 Pyroelectric Generators

The pyroelectric effect is the property of certain crystalline materials to generate an electric potential when subjected to a change in temperature over time. As described in [10, 11], these materials have permanent dipole moments throughout their crystal structure. When the material undergoes a homogeneous change in temperature, the crystal's dipoles align in one direction, producing a net voltage. Leaving the crystal at a constant temperature causes free charges at the crystal surface to be neutralized by an internal depolarization field. This is analogous to the piezoelectric effect, in which a change in strain is required, rather than simply a strain.

The pyroelectric effect has been closely tied to materials that demonstrate piezoelectric properties. All known classes of pyroelectric crystals demonstrate the piezoelectric effect when subjected to mechanical stress [11, 12]. Of the 32 crystal classes, 20 produce an electric field when subjected to mechanical stress (piezoelectricity). Of these 20 classes, 10 also demonstrate an electric field when subjected to a time varying temperature (pyroelectricity).

When a pyroelectric device is heated or cooled and undergoes thermal expansion/contraction, it also undergoes strain. This causes generation of a secondary voltage potential, due to the piezoelectric effect. For some materials (including many of the linear pyroelectric materials) the pyroelectric effect accounts for less than 5 %, with the remainder caused by the piezoelectric effect [13].

Traditionally, materials showing pyroelectric properties have predominantly been used as sensors. Examples include sensors for hydrogen detection [14], temperature variation [15], and monitoring airflow through a human respiratory system [16]. When these same materials have been used in energy harvesting applications, it is typically their piezoelectric properties that have been used, rather than their pyroelectric effect. Given the current interest in energy harvesting and its applications to remote small-scale devices, such as sensor networks, the pyroelectric effect has recently been the subject of significant research.

5.2.1 Pyroelectric Cycles

One of the major drawbacks to practical devices that can harvest energy from pyroelectric materials is that to generate an electric field, the device's temperature must change with time. In contrast, thermoelectric devices require only a temperature differential to be maintained: a situation that can often be achieved passively through the use of cooling devices such as heat sinks.

Few practical situations will provide an external temperature that varies sufficiently to generate a significant voltage from a pyroelectric device. Consequently, a temperature gradient is often converted to a temperature variable in time through the use of a working fluid pumping between hot and cold reservoirs, as described by Sebald et al. [17]. This system is then coupled with one of several thermodynamic cycles to optimize the harvested energy. These cycles typically involve controlling the thermal connection to the external temperature reservoirs, as well as the electrical load, to draw energy from the device at an appropriate point in the cycle. The cycle chosen will significantly influence the potential operating efficiency of the system, as shown analytically by Sebald et al. [17].

Of several thermodynamic cycles analyzed theoretically by Sebald et al. [17], the most promising is the Synchronized Switch Damping on Inductor (SSDI) cycle. The SSDI cycle operates in a similar way to power-electronics solutions, in that it uses an inductor on the output of the device, and inverts the load at the minimum temperature. The authors claim that realistic efficiencies of up to 50 % of the Carnot limit are possible with appropriate engineering and material selection.

5.2.2 Performance of Pyroelectric Energy Generators

In recent years, several attempts have been made to produce a viable thermal energy harvester using pyroelectric materials. Xie et al. [18] introduce a method by which the output voltage and power of a single pyroelectric generator can be modeled. The method is based on the pyroelectric coefficient of the material, the surface area of the electrodes, the internal capacitance of the material, and the values of the electrical components external to the device. In experimental replication, the generator undergoes only half of a temperature cycle; however, the measured output voltage is within 4 % of the predicted value for the duration of the cycle. The output power of this device peaks at approximately 0.35 μW/cm^2, although this is using a relatively slow heating cycle (14.45 K/s). The electrical circuit uses components designed to maximize the output voltage, rather than power.

Ravindran et al. [19] demonstrate a more realistic pyroelectric generator. A heat engine allows heat to be transferred from a hot reservoir to a cold reservoir, with an oscillating diaphragm that ensures a continuously changing temperature of the pyroelectric material. While the precise heating rate is not shown, it can be inferred at least on the cooling side of the cycle, as the maximum delta-T value of 79.5 K occurs in less than one second, a significant increase over [18]. This results in maximum open-circuit voltages of approximately 13 V, and an average power output of 3.03 μW/cm^2: an order of magnitude greater than that of [18]. Both papers [18, 19] indicate that pyroelectric materials should continue to function up until their Curie temperature. This is dependent on the material, but is in the order of 165 °C for the material polyvinylidene fluoride (PVDF), and 350 °C for lead zirconium titanate (PZT), as shown in [18].

The major advantage of pyroelectric devices for energy harvesting over traditional thermoelectric devices is that—with proper engineering—substantially higher thermoelectric efficiencies are possible through optimizing the heat cycle. However, these efficiencies are yet to be demonstrated in practice. The major drawback to pyroelectric energy harvesters is the need to operate a heat cycle that will allow for a time varying temperature, e.g. through the use of working fluids.

5.3 Seebeck Thermoelectric Generators

The field of thermoelectric generators is well established, with various mechanisms to generate electricity directly from thermal differences. The process of thermoelectric generation is governed by the Seebeck effect (after physicist Thomas Johann Seebeck). Devices exhibiting the Seebeck effect typically consist of two materials: an n-type and a p-type semiconductor (e.g. bismuth telluride, bismuth selenide). The two semiconductors produce electricity directly when their junctions are exposed to a temperature difference. The two individual materials

have a property called the Seebeck coefficient $S(T)$. The n-type material has a negative Seebeck coefficient, while the p-type has a positive Seebeck coefficient.

Seebeck generators produce voltage in proportion to both the temperature difference between the hot and cold side, and the difference between the two materials' Seebeck coefficient. Typically, the two semiconductors are connected electrically in series, but thermally in parallel. Junctions between the two materials are alternately connected to hot and cold sides via electrical insulators, as shown in Fig. 5.2.

The flow of heat energy from the hot side to the cold side diffuses the charge carriers from the hot side to the cold side. Because the n-type material has an excess of negative charge carriers, a conventional current is produced from the cold side to the hot side. The p-type material has an excess of positive charge carriers, and thus conventional current flows from the hot to the cold side. This overall movement causes a current to flow through an external circuit.

The Seebeck coefficient is a measure of the voltage produced for a unit temperature rise across a material. The Seebeck coefficient is itself a function of temperature. The magnitude of the voltage for a Seebeck device, V can be calculated using:

$$V = \int_{T_L}^{T_H} S_1(T) - S_2(T) dT$$

where T_H and T_L are the high and low absolute temperatures, respectively, and S_1 and S_2 are the two materials' Seebeck coefficients.

As the voltage from this thermocouple is small, a number of modules are connected in series to achieve useful voltages.

Up until 2000, the efficiencies of thermoelectric generators were quite low. This is because the material needed to be both a good electrical conductor and a good thermal insulator to be effective as a thermoelectric device. Most materials that are good electrical conductors are also good thermal conductors; equally, those materials that offer good thermal insulation are usually electrical insulators. For thermoelectric materials, a figure of merit, ZT, was devised:

$$ZT = \frac{\sigma S^2}{\lambda} \left(\frac{T_H - T_L}{2} \right)$$

Fig. 5.2 A thermoelectric module internal structure (note the series connection of each p–n junction pair)
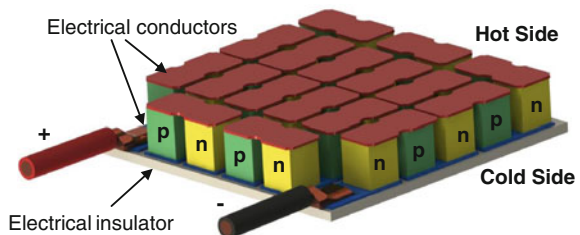
where σ is the electrical conductivity, λ is the thermal conductivity, and S is the Seebeck coefficient.

Although ZT is theoretically unlimited, until very recently, ZT values were approximately one. However, with efficiency drivers pushing research into waste heat capture some research has identified materials with ZT values of three–four [20, 21]. More recent research has identified classes of nanomaterials—often existing materials that have been mechanically ground to a small size—that have higher ZT values [22–25].

Higher ZT values may allow practical and cost-effective implementation of thermoelectric converters in commercial applications. At values of ZT around one, efficiency of energy generation is around 5–12 % of the Carnot limit [26]. Doubling this ZT value will increase the efficiency to 25 % of the Carnot limit. For more information on the current state-of-the-art of thermoelectric power generation, see Weiling and Shantung [27], and Riffat and Ma [26].

5.3.1 Applications of Seebeck Devices

The use of Seebeck devices in the low-temperature region has been explored in [28–30]. In some of these experiments, a miniature greenhouse was designed that elevated the ambient temperature of the hot side, while the cold side was attached to water-immersed heat sink. A variety of capture areas, electrical circuits and dome designs were tested. At ambient conditions around 300 K, the hot side was elevated to 350 K and generated more than 14 mW. A similar design based in soil was investigated in [31].

In the medium-temperature range, a focus of research and commercial development has been the application of Seebeck devices in vehicle exhaust systems. Some of these produce quite large power outputs, and could conceivably be used to replace the alternator [32, 33] or the vehicle air-conditioning equipment [34].

Of additional interest in the medium-temperature range are radioisotope thermoelectric generators. These very-high-power devices have thermal outputs between 200 and 2000 W, and have been deployed mainly to remote systems. The source of power is a radioisotope, such as plutonium (in the form PuO_2), which decays by beta radiation. The radiation is absorbed by a surface that converts the kinetic energy of the decay product into heat, which feeds an array of thermocouples to generate electricity. These systems have been deployed in interplanetary probes (*Voyager* I and II, *Galileo* and *Cassini*) [35]. They have also been used by both the former Soviet Union (using strontium as the source) and the United States' armed forces for deployment to remote radar stations [36]. Due to efficiencies of less than 8 %, the electrical output of these systems is modest, rarely exceeding hundreds of watts. For example, the *Viking* program used a System for Nuclear Auxiliary Power (SNAP-19). This produced 43 W of electrical power from 525 W of thermal power [37].

In the high-temperature region, thermoelectric effects have been found with some more exotic materials. Generally the figure of merit, ZT, at these temperatures is lower than has been found at more modest temperatures. Fujita et al. [38] studied single crystals of sodium and cobalt oxide complexes and found ZT numbers exceeding one at temperatures up to 800 K. Ohta et al. [39] researched niobium-doped strontium titanate (SrTiO) and found ZT values up to 0.38 at 1000 K.

5.4 Alkali Metal Thermal-to-Electric Converters

The alkali metal thermal-to-electric converter (AMTEC) process is a thermally regenerative electrochemical device that converts heat to electricity. The process works due to the unique properties of a material called beta alumina solid electrolyte (BASE). BASE has the ability to conduct alkali metal ions, such as sodium ions (Na^+), but does not readily conduct atoms or electrons. The AMTEC device was originally called a sodium heat engine, because the alkali metal used was sodium. However, other alkali metals, such as potassium, can also operate successfully in the cycle. The AMTEC operates via a modified Rankine cycle [40].

The BASE is used as a thin barrier between two thermoelectric conversion chambers. In one chamber, heat transforms an alkali metal liquid to a high-pressure vapor via an evaporator. As shown in Fig. 5.3, the vapor, which is in contact with the BASE, causes a vapor-pressure differential across the BASE barrier. The vapor pressure difference drives the alkali ions through the BASE into the second chamber, which contains low-pressure vapor. Waste heat is lost from this second chamber via a condenser. The low-pressure chamber collects the alkali metal ions transferred from the high-pressure chamber, creating a positive electrical charge. An electrical load can be placed across the two chambers, drawing the electrons from the low-pressure, negatively charged chamber and delivering them to the positively charged chamber [41]. To complete the cycle, an electromagnetic pump returns the alkali metal from the positive side of the membrane to the negative side.

Many publications have explored AMTEC devices. The research is largely driven by the space exploration industry, which requires long-lasting, reliable energy production for extended space travel. The Jet Propulsion Laboratory has published much work surrounding AMTEC devices, e.g. [42–48]. Underwood et al. [43] predicts power densities of 15–18 W/kg for 100 W output. The overall efficiency of an AMTEC device has been reported to be as high as 18 %, which corresponds to 89 % of the Carnot limit [41]. Hot side working temperatures for AMTEC systems tend to range from 900–1300 K, with cold side temperatures from 400–800 K. The cold side temperature must be above about 371 K to prevent the sodium solidifying [49].

Advantages of AMTEC devices include high reliability due to an absence of moving parts, and high efficiency [43]. Disadvantages include power degradation,

Fig. 5.3 Schematic of an alkali metal thermal-to-electric converter device
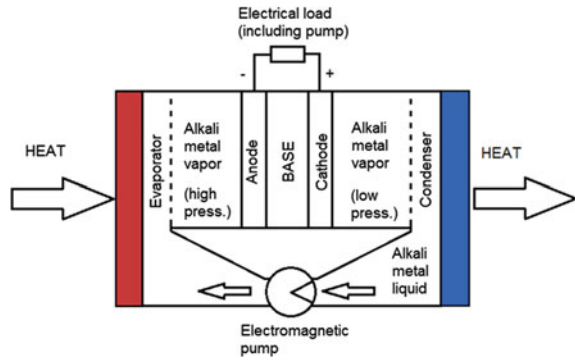
due to 'clogging' of membranes with the working fluid, and high operating temperatures [50].

5.4.1 Potential of AMTEC at MEMS Scale

The authors do not know of any AMTEC device that has ever been produced at MEMS scale. Most of the research into AMTEC is driven by the need for macro-scale devices for the space exploration industry. To our knowledge, there is currently no interest in miniaturization of this technology.

5.5 Johnson Electro Mechanical Systems

The Johnson Electro Mechanical Systems company has developed several thermally driven electrochemical generators. Of particular interest are the Johnson Thermo Electrochemical Converter (JTEC) and the Johnson Electric Heat Pipe (JEHP).

5.5.1 Johnson Thermo Electrochemical Converter System

The JTEC is similar to the AMTEC device, in that a pressure differential caused by heat is used to drive positive ions (hydrogen ions/protons in the case of JTEC) through a membrane, thus creating an electrical charge across the membrane.

The JTEC uses high-pressure hydrogen, which is forced through a membrane electrode assembly (MEA). The MEA is comprised of a proton exchange membrane sandwiched between two electrodes. The high-temperature 'power stage' MEA splits the hydrogen into protons and electrons. The protons pass through the

membrane, and the electrons leave via the electrodes to perform work. Protons are returned to the low-temperature 'compression stage' side of the device, where electrical energy input into a second MEA allows protons to reform to hydrogen atoms.

Johnson claims the JTEC device follows the Ericsson thermodynamic cycle [50]. The amount of energy the device can generate is the difference in electrical energy required to compress the hydrogen at low temperature, and the electrical energy generated by the hydrogen passing through the MEA at high temperature. The working temperatures for this device are not specifically known. However, [51] describes the device as working at 'relatively low temperatures', having previously described other thermoelectric conversion cells operating between 1200 and 1500 K. It can therefore be safely assumed that the operating temperatures will be below 1200 K. Further, the patent states the engine 'may be operated over relatively low temperature differences'. The efficiency of a JTEC device has been quoted as 31.25 % solar conversion efficiency [52].

5.5.2 Johnson Electrochemical Heat Pipe

The JEHP is similar to the JTEC in that a pressure differential caused by heat is used to drive hydrogen ions/protons through a membrane, thus creating an electrical charge across the membrane. As in the case of the JTEC, the high-pressure hydrogen is forced through a MEA. However, the JEHP device contains a 'binary working fluid, which is comprised of hydrogen in combination with a two-phase fluid' [40]. As a power generator, heat applied to the liquid binary working fluid causes the fluid to vaporize (absorbing the heat), creating a low hydrogen partial pressure.

Very little information seems to be available on this technology. It is not known whether existing or further research into this form of energy generation is occurring.

5.5.3 Potential of JTEC and JEHP at MEMS Scale

No evidence of a prototype of either device at MEMS scale has been published, but it seems entirely feasible that this technology could be created to work at this scale. The JTEC researchers state:

> 'The engine is scalable and has applications ranging from supplying power for Micro Electro Mechanical Systems (MEMS) to power for large-scale applications such as fixed power plants' [50].

5.6 Infrared Photovoltaic Harvesters

Photovoltaic (PV) modules represent the most successful method to date of directly converting light—typically solar radiation—into electrical energy. The operation of photovoltaic cells is well documented. When photons of light of sufficient energy (known as the band gap of the photovoltaic material) hit a PV cell, an electron is released from the surrounding material, causing the cell to generate a voltage. The voltage (and hence electrical power) generated by a cell is directly related to the minimum photon energy required to release electrons. If a photon does not have sufficient energy, it will not cause an electron to be released; if its energy is higher than the material's band gap, any additional energy is re-emitted as light and heat, and is therefore wasted.

Most modern PV cells are based on silicon, which has a band gap of 1.11 eV [53]. This corresponds to a photon wavelength of 1100 nm. Consequently, most PV cells are limited to incident light with a frequency not much below that of the visible portion of the spectrum (400–700 nm) or higher. However, more than 50 % of the incident radiation at Earth's surface is in the infrared spectrum (700–3000 μm). A significant majority of this longer-wavelength radiation is not harvested by typical silicon-based PV cells, limiting their efficiency to approximately 34 % [54].

Several techniques have been developed that can extend the silicon band gap into the infrared range. PV systems capable of converting infrared light into electrical energy—and in particular, systems devoted specifically to harvest light energy from combustion—have been in development since the 1950s [55].

Thermo-photovoltaic (TPV) devices typically use fuel combustion to heat an emitter material to temperatures at which it will emit thermal radiation, in the form of infrared light (Fig. 5.4). The infrared light can be harvested by PV cells targeted at the infrared portion of the spectrum. While early TPV devices were hindered by cripplingly low efficiencies, recent advances in PV technology have increased the viability of this technique for thermal energy harvesting.

One limitation of the photovoltaic effect is due to the specific band gap of photovoltaic materials. The band gap determines both the minimum energy required for a photon to promote an electron into the conduction band, and the electrical energy that a single electron can expend on a load. A lower band gap will allow lower-frequency incident light to energize valence electrons in the material, potentially increasing the power output of the device. However, as any additional energy in the photon is effectively discarded, too low a band gap can reduce the output power of a PV cell. The contained energy of an electron is directly proportional to its frequency (known as Planck's relation); hence, the frequency spectra of incident light on a PV cell directly influences its power output.
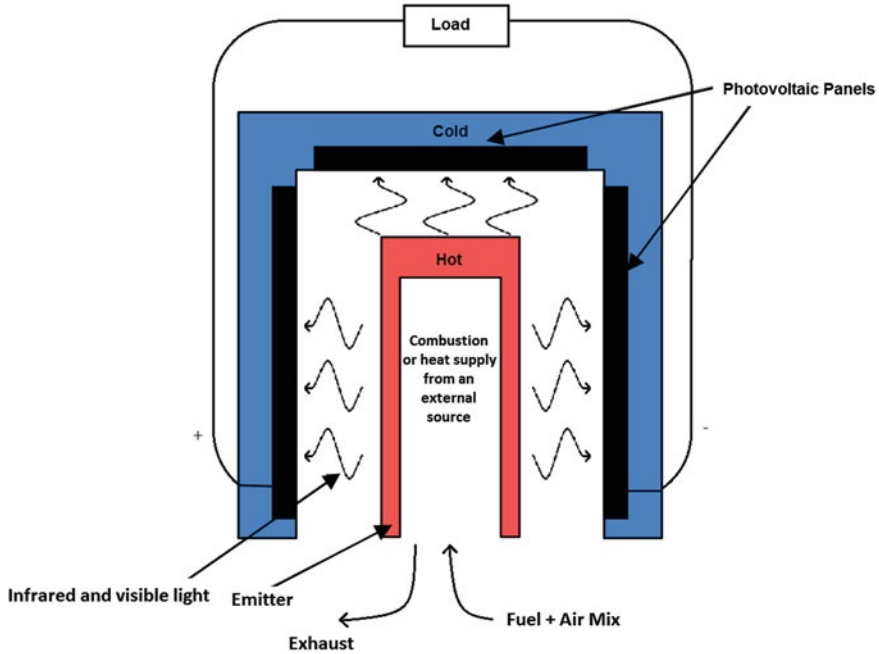
Fig. 5.4 IRPV-based thermal energy harvester

As the vast majority of commercial PV applications involve harvesting solar energy, the majority of research has focused on improving the ability of PV cells to absorb more light in the infrared spectrum. Due to the optimal band gap being close to the visible light region, and technical and economic limitations, focus on improving the absorption of infrared light by PV cells has been limited. However, some progress has been made using different methods, as detailed below.

5.6.1 Multi-junction PV

As the wavelength spectrum of incident light onto Earth's surface is well understood, it is possible to analytically determine the ideal band gap of a single-junction PV system [54], along with the maximum theoretical efficiency at that band gap [56]. Under the standard solar spectrum known as AM1.5 [57], the ideal band gap has been calculated to be 1.34 eV. This is only slightly higher than that of silicon, which may have contributed to the popularity of silicon-based PV cells. The corresponding limiting efficiency, approximately 29 % for silicon cells, is known as the Shockley-Queisser limit.

The above-stated ideal band gap is only ideal when considering a single-junction cell. One of the most common methods of extending the accessible

spectrum of PV cells is through the use of multi-junction, or tandem, cells. Tandem cells contain several layers of PV material with different band gaps. The material with the highest band-gap is closest to the top, and the band gap progressively decreases for each successive layer. Any light with insufficient energy to promote an electron in one layer will pass through the material until it reaches a layer that can absorb the photon.

This method has the advantage of extending the absorption spectrum of a PV cell into the longer-wavelength range and increasing the output voltage of the cell. Using the Shockley and Queisser method, for a given number of layers, the optimal band gaps and theoretical efficiency are both calculable [54]. For an infinite number of layers, the maximum theoretical efficiency approaches 86 %. Each new layer, however, comes with significant complexity and manufacturing cost. For this reason, only a small number of multi-junction PV cells have been brought to market so far.

5.6.2 Quantum-Dot PV

A PV technology generating some interest currently is the quantum-dot device [58]. The term refers to a nano-crystalline semiconductor incorporated into a standard matrix material. The size and shape of the nano-crystal affects the band gap of the device, which typically increases as the crystal is made smaller. The band gap of the solar cell can thus be tuned by varying the size of the crystal, allowing the cell to be optimized for the terrestrial solar spectrum.

5.6.3 Organic Solar Cells

A different way of optimizing the band gap of a solar cell is the customized synthesis of organic semiconducting materials. Organic solar cells (OSC) have been the subject of significant research in the past decade. OSC systems are subject to similar issues regarding single-junction and multiple-junction systems as described in Sect. 5.7.1. In an OSC system, electrons and holes are separated by an electric field due to the difference in work function of the cell's electrodes. However, layers that are thick enough for good absorption are subject to significant charge recombination. When an electron and hole pair, an exciton, are formed near the interface between different materials, the electron can transfer to the second (electron accepting) semiconductor, leaving the hole to travel in the donor semiconductor [59]. OSC systems show promise in thermal energy harvesting, due to the variety of potential materials with differing band gaps available to customize a PV cell to the desired requirements.

5.6.4 Energy Harvesting Applications

There appears to have been little investigation into the practical energy-harvesting capability of infrared photovoltaic panels. Several patents [60, 61] have demonstrated the capability to harvest thermal energy from a fuel-fired emission source. In both these cases, however, an emission of at least 1300 K is expected, with efficiencies dropping off significantly at lower temperatures. This range is well outside the typical temperature that can be expected from most waste-heat recovery applications.

Silicon-based PV at the MEMS scale has been proposed several times [62, 63], but these approaches all suffered from the band gap limitations of silicon PV as described in Sect. 5.7. OSC have more recently been attempted at the MEMS scale [64], and show some promise, although the focus is not yet on operating these systems in the infrared portion of the spectrum.

The main drawbacks of infrared PV/TPV at the MEMS scale will be similar to those at the macro-scale. The largest drawback is the very low efficiency with which infrared PV typically operates, which is exacerbated by the low amounts of power expected to be available at the MEMS scale. In addition, TPV devices tend to lose a portion of their thermal energy to exhaust gases and insulation losses, typically around 40 % [65] for kilowatt-scale systems. This could reasonably be expected to be worse for MEMS-scale devices, further limiting their potential efficiency.

References

1. Dorf RC (2006) Systems, controls, embedded systems, energy, and machines, 6th edn. CRC Press, Boca Raton
2. Richardson OW (2003) Thermionic emission from hot bodies, 1st edn. Wexford College Press, Palm Springs, p 332
3. Myatt J (1963) Thermionic emission from zirconium carbide with caesium vapour present. Adv Energy Convers 3(1):279–285. ISSN: 0365-1789
4. Da Rosa A (2009) Fundamentals of renewable energy processes, 3rd edn, pp 219–262
5. Gryaznov GM, Zhabotinskii EE, Zrodnikov AV et al (1989) Thermoemission reactor-converters for nuclear power units in outer space. At Energy 66:414–418
6. Zavadil K, King D (2001) Thin film dispenser cathodes for thermionic micro-devices. MRS Proc 691:G113 691. doi:10.1557/PROC-691-G11.3
7. Zhang C, Najafi K, Bernal LP, Washabaugh PD (2003) Mechanical and thermal design of a combustion-based thermionic micro power generator. In: ASME conference proceedings 2003, pp 717–724. doi:10.1115/IMECE2003-41531
8. Tavkhelidze A, Svanidze V, Noselidze I (2007) Fermi gas energetics in low-dimensional metals of special geometry. J Vac Sci Technol B Microelectron Nanometer Struct 25:1270–1275
9. Kilgrow S, Geirsson A, Sigfusson T (2003) Harnessing of low temperature geothermal and waste heat using power chips in Varmaraf heat exchangers. In: International geothermal conference, Reykjavik, Iceland, p 097

10. Hossain A, Rashid MH (1991) Pyroelectric detectors and their applications. IEEE Trans Ind Appl 27:824–829
11. Whatmore RW (1986) Pyroelectric devices and materials. Rep Prog Phys 49:1335–1387
12. Bogdanov SV (2002) The origin of the piezoelectric effect in pyroelectric crystals. IEEE Trans Ultrason Ferroelectr Freq Control 49:1469–1473
13. Tichý J, Erhart J, Kittinger E, Prívratská J (2010) Fundamentals of piezoelectric sensorics: mechanical, dielectric, and thermodynamical properties of piezoelectric materials. Springer, Berlin
14. Christofides C, Mandelis A (1990) Solid state sensors for trace hydrogen gas detection. J Appl Phys 68:R1–R30
15. Lang SB, Steckel F (1965) Study of the ultrasensitive pyroelectric thermometer. Rev Sci Instrum 36:1817–1821
16. Huang YP, Young MS, Tai CC (2008) Noninvasive respiratory monitoring system based on the piezoceramic transducer's pyroelectric effect. Rev Sci Instrum 79:35103–351039
17. Sebald G, Lefeuvre E, Guyomar D (2008) Pyroelectric Energy Conversion: Optimization Principles. IEEE Trans Ultrason Ferroelectr Freq Control 55:538–551
18. Xie J, Mane XP, Green CW et al (2010) Performance of thin film piezoelectric materials for pyroelectric energy harvesting. J Intel Mater Syst Struct 21:243–249
19. Ravindran SKT, Huesgen T, Kroener M, Woias P (2011) A self-sustaining micro thermomechanic-pyroelectric generator. Appl Phys Lett 99:104102–1041023
20. Venkatasubramanian R, Siivola E, Colpitts T, O'Quinn B (2001) Thin-film thermoelectric devices with high room-temperature figures of merit. Nature 413:597
21. Harman TC, Taylor PJ, Spears DL, Walsh MP (2000) Thermoelectric quantum-dot superlattices with high ZT. J Electron Mater 29:L1–L2
22. Chen HY, Savvides N (2009) Microstructure and thermoelectric properties of n- and p-type Mg2Sn compounds prepared by modified Bridgeman method. J Electron Mater 38:1056–1060
23. Chuang L, Savvides N, Tan TT, Li S (2010) Thermoelectric properties of Ag-doped Mg2Ge thin films prepared by magnetron sputtering. J Electron Mater 39:1971–1974. doi:10.1007/s11664-009-1052-4
24. Muller KH (2010) Modeling thermoelectric properties of assemblies of nanocrystals. In: International conference on nanoscience and nanotechnology, Sydney, Australia, p 5
25. Ferrari M, Ferrari V, Guizetti M et al (2007) Characterization of thermoelectric modules for powering autonomous sensors. In: 24th IEEE instrumentation and measurement technology conference, Warsaw, Poland, pp 1708–1713
26. Riffat SB, Xiaoli M (2003) Thermoelectrics: a review of present and potential applications. Appl Therm Eng 23:913–935
27. Weiling L, Shantung T (2004) Recent developments of thermoelectric power generation. Chin Sci Bull 49:1212–1219
28. Knight C, Collins M (2009) Results of a water based thermoelectric energy harvesting device for powering wireless sensor nodes. In: SPIE, p 72880Y–12
29. Davidson J, Collins M, Behrens S (2009) Thermal energy harvesting between the air/water interface for powering wireless sensor nodes. In: Ahmadian M, Ghasemi-Nejhad MN (eds) SPIE. pp 728814–11
30. Knight C, Davidson J (2010) Thermoelectric energy harvesting as a wireless sensor node power source. SPIE, p 76431E−11
31. Stevens J (2004) Optimal placement depth for air-ground heat transfer systems. Appl Therm Eng 24:149–157
32. LaGrandeur J, Crane D, Eder A (2005) Vehicle fuel economy improvement through thermoelectric waste heat recovery. In; Proceedings of the 11th diesel engine emissions reduction
33. Thacher EF, Helenbrook BT, Karri MA, Richter CJ (2007) Testing of an automobile exhaust thermoelectric generator in a light truck. J Autom Eng 221:95–107
34. Yang J (2009) Automotive applications of thermoelectric materials. J Electron Mater 38:1245

35. Anon Voyager Mission Operations Status Reports. http://voyager.jpl.nasa.gov/mission/weekly-reports/index.htm. Accessed 11 Dec 2012
36. Rumyantsev A (2003) Report by minister of atomic energy alexander rumyantsev at the IAEA conference "security of radioactive sources". http://www.iaea.org/newscenter/features/radsources/pressbriefing.html. Accessed 28 Jan 2011
37. Bennet GL (2006) Space nuclear power: opening the final frontier. In: 4th international energy conversion engineering conference and exhibit, San Diego, CA, pp 26–29
38. Fujita K, Mochida T, Nakamura K (2001) High-temperature thermoelectric properties of NaxCoO2-δ single crystals. Jpn J Appl Phys 40:4644
39. Ohta S, Takashi N, Ohta H et al (2005) Large Thermoelectric performance of heavily Nb-doped SrTiO3 epitaxial Film at high temperature. Appl Phys Lett 87:092108. doi:10.1063/1.2035889
40. Johnson HP (2012) http://www.johnsonems.com/?q=node/5. Accessed 13 Nov 2012
41. Vining C, Williams R, Underwood M, Al E (1993) Reversible thermodynamic cycle for amtec power conversion. J Electrochem Soc 140:2760–2763
42. Ryan M, Williams R, Lara L (2001) Advances in electrode materials for amtec. In: Space Technology and Applications International Forum, pp 1088–1093
43. Underwood ML, Mondt J (1997) AMTEC for space radioisotope power applications. http://trs-new.jpl.nasa.gov/dspace/handle/2014/22008. Accessed 28 May 2013
44. Ryan MA, Williams RM, Fiebig G et al (2002) Mo/NaxTiO2 mixed conducting electrodes the alkali metal thermal to electric converter. California Institute of Technology, Pasadena
45. Shields VB, Kisor AK, Fiebig B et al (2001) Metallurgical examination of an AMTEC power unit. In: Space Technology and Applications International Forum-2001. AIP Conference Proceedings, pp 1094–1099
46. Ryan MA, Williams RM, Lara L et al (1999) The role of titanium dioxide in the performance of titanium nitride AMTEC electrodes. California Institute of Technology, Pasadena
47. Ryan MA, Kisor A, Williams RM et al (2000) Lifetimes of electrodes for AMTEC cells. In: AIP conference proceedings. Space Technology and Applications International Forum, pp 1377–1382
48. Ryan M, Shields V, Cortez R (2000) Lifetimes of AMTEC electrodes: molybdenum, rhodium-tungsten, and titanium nitride. Space Technol Appl Int Forum 2:1377–1382
49. Lodhi M, Vijayaraghavan P, Daloglu A (2001) An Overview of advanced space/terrestrial power generation device: AMTEC. J Power Sour 103:25–33
50. Johnson Thermo-Electrochemical Converter System. http://www.johnsonems.com/?q=node/2. Accessed 13 Nov 2012
51. Johnson LG, Muller JR (2007) Johnson reversible engine. EP1314214A1
52. Moseman A (2013) Energy Startups cite collaboration, govt. funding to fulfill promise. In: Popular mechanics. http://www.popularmechanics.com/science/environment/green-energy/4287514?series=60?series=60. Accessed 28 May 2013
53. Streetman BG, Banerjee S (1995) Solid state electronic devices. Prentice-Hall, Englewood Cliffs
54. Marti A, Arafijo GL (1996) Limiting efficiencies for photovoltaic energy conversion in multigap systems. Sol Energy Mater Sol Cells 43:203–222
55. Nelson RE (2003) A brief history of thermophotovoltaic development. Semicond Sci Technol 18:S141–S143. doi:10.1088/0268-1242/18/5/301
56. Shockley W, Queisser HJ (1961) Detailed Balance limit of efficiency of p-n junction solar cells. J Appl Phys 32:510–519
57. Emery K, Solar spectral irradiance: air mass 1.5. In: American society for testing and materials. http://rredc.nrel.gov/solar/spectra/am1.5/#about. Accessed 11 Mar 2013
58. Barnham KWJ, Duggan G (1990) A new approach to high-efficiency multi-band-gap solar cells. J Appl Phys 67:3490. doi:10.1063/1.345339
59. McGehee MD, Topinka MA (2006) Solar cells: pictures from the blended zone. Nat Mater 5:675–676

60. Fraas LM, Samaras JE, Baldasaro PF, Brown EJ (1995) Spectral control for thermophotovoltaic generators. US5403405
61. Kovacik G, Fraas L, Astle C (2003) Thermiphotovoltaic Device. US 2006/0107995A1
62. Lee JB, Chen Z, Allen MG et al (1995) A miniaturized high-voltage solar cell array as an electrostatic MEMS power supply. J Microelectromech Syst 4:102–108. doi:10.1109/84.465125
63. Bermejo S, Ortega P, Castañer L (2005) Fabrication of monolithic photovoltaic arrays on crystalline silicon by wafer bonding and deep etching techniques. Prog Photovoltaics Res Appl 13:617–625. doi:10.1002/pip.615
64. Lewis J, Zhang J, Jiang X (2009) Fabrication of organic solar array for applications in microelectromechanical systems. J Renew Sustain Energy 1:13101
65. Schaevitz S (2000) A MEMS thermoelectric generator. Ph.D. dissertation, pp 1–165

Index